Study of Photoluminescence from Amorphous and Crystalline Silicon Nanoparticles

Synthesized using a Non-Thermal Plasma

by

Prateek Garg

A Thesis Presented in Partial Fulfillment
of the Requirements for the Degree of
Master of Science

Approved July 2015 by the
Graduate Supervisory Committee:

Zachary C. Holman
Yong Hang Zhang
Mariana Bertoni

ARIZONA STATE UNIVERSITY

August 2015

ABSTRACT

High photoluminescence (PL) quantum yields reported from amorphous (a-Si) and crystalline (c-Si) nanoparticles have opened up lots of possibilities for use of silicon in optical applications such as light emitting diodes (LEDs), photonics and solar cells with added processing and cost benefits. However, the PL response and the mechanisms behind it are highly dependent on the matrix in which the nanoparticles are grown and on the growth method. While, the bottom-up approach for deposition of free standing nanoparticles seem to be perfectly suited for large area deposition for LED and solar cell applications, the dominant growth techniques (laser ablation and pyrolysis) have been shown to suffer from limitations in control over size distribution of nanoparticles and the requirement of equipment capable of withstanding high temperature. This led to the exploration of plasma based synthesis methods in this work.

Towards this effort, the development and automation of a novel tool "Anny" for synthesis of silicon nanoparticles using non-thermal plasma chamber is reported. These nanoparticles are then accelerated due to choked flow through a nozzle leading to substrate independent deposition. The nanoparticle properties are characterized against precursor gas flow rates and RF power to identify the optimum growth conditions for a stable, continuous deposition. It is found that amorphous nanoparticles offer a wide variety of chamber conditions for growth with a high throughput, stable plasma for continuous, long term operations.

The quantum confinement model for crystalline and spatial confinement models for amorphous nanoparticles in our size regime (6-8nm) are suggested for free standing

i

nanoparticles and we report a high PL output from well passivated amorphous nanoparticles.

The PL output and its dependence on stability of surface hydrogen passivation is explored using Fourier Transform Infrared spectroscopy (FTIR). It is shown that the amorphous nanoparticles have a better and more stable passivation compared to crystalline nanoparticles grown under similar conditions. Hence, we show a-Si nanoparticles as exciting alternatives for optical applications to c-Si nanoparticles.

To my parents

ACKNOWLEDGEMENTS

First of all, I would like to thank my research adviser, Dr. Zachary Holman. His passion, dedication and commitment towards his research continued to always encourage me to work harder. He showed me the importance of keeping an eye out for new ideas and helped me appreciate the significance of hands-on work to realize a scientific idea to an engineering solution. His direction and guidance were instrumental in the evolution of this work to its current form.

I am also very thankful to my thesis committee, Dr. Yong-Hang Zhang and Dr. Mariana Bertoni for taking time out from their busy schedule to guide and help to improve this work. Their knowledge in their respective fields is highly respected and I am honored to have them in my committee.

I would also like to thank my labmates: Peter, Joe, Priyaranga, Salman and Matt for their help in the experimental sections and for their discussions and support which helped shape this thesis. I would also like to thank Laura for her extensive help in PL measurements using the Renishaw tool.

Last but not the least, I would like to thank my family who have been the pillars of support throughout my life.

To my mother, who helped me keep on going during difficult times with her never-ending words of encouragement and support.

To my father, who always inspired me to be the best I can be, and nothing less. Thank you for encouraging me to continuously keep on improving and to never give up.

TABLE OF CONTENTS

LIST OF TABLES

LIST OF FIGURES

Chapter 1

INTRODUCTION

Motivation

Silicon has been the driving force behind the microelectronics industry for the last 50 years leading to the ubiquitous nature of high computing power all around us. The improvements in process technology of silicon have led to a cost reduction of the order of 10^7 [1] for individual transistors leading to windfall gains for other silicon based industries such as photovoltaics.

With the scaling of transistors to sub 10 nm regime, the delays due to traditional interconnect are emerging as a limit to IC operation at high frequency requiring the development of photonics based components based on optically active materials. Cheap, optically active semiconductors are also necessary to bring down the costs of optical devices which require large area film coatings such as solar cells and LEDs [2,3]. Potential use of silicon based structures for these applications would help towards this goal. However, one of the major hurdles in this and other optoelectronic applications for silicon is its indirect bandgap, necessitating the reliance on direct bandgap III-V or II-VI (or more recently organic) compounds. In addition to the intrinsic material limitations of cost, availability and toxicity, these compounds are also not easily integrated into the silicon based ICs further raising cost. The integration of optical components into the silicon IC, enabling the design and fabrication of smaller, cheaper system on chips has been identified as a major crux area by the ITRS in its More than Moore (MtM) model [4] governing the evolution of the semiconductor industry over the next few years. This is a field where the

high photoluminescence properties of silicon nanoparticles have a huge potential to contribute the direction of the industry growth in the future.

Silicon based nanostructures and nanoparticles have emerged as an exciting field of research since the discovery of strong photoluminescence from porous silicon in the early 90's [5]. The applicability of silicon nanoparticles for LED applications has been further reinforced by the demonstration of electroluminescence in silicon nanoparticles [6].

Another exciting application for nanoparticles is as a wavelength red-shifter for a-Si/c-Si heterojunction solar cells. In heterojunction solar cells, a-Si is deposited on silicon to reduce surface recombination. However, a-Si leads to parasitic absorption in the blue and UV region. Hence, silicon nanoparticles can be used which absorb these short wavelength light (as shown using a sample from our lab in figure 1) and reemit light near 800-900nm (discussed later) which is absorbed by the wafer and can be used to generate electron hole pairs, leading to a higher short circuit currents in the cell.
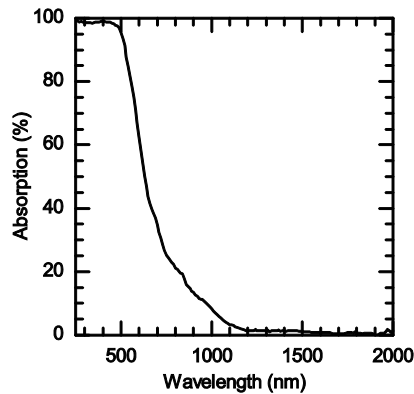
Figure 1 Absorption spectrum for an a-Si silicon nanoparticles sample from the deposition system at Holman Lab

These potential applications have led to numerous studies by a number of groups over the last two decades to understand the origin of such a high PL from an indirect semiconductor, and to use the improved understanding to achieve a higher tunability and

quantum yields of the PL. Most of the research in the field has been focused on the top-down approach of etching away SiOx or SiNx layers to obtain structured nanoparticles in the respective matrices. This approach, while suitable for the high precision application such as quantum dot transistors, fares poorly for applications such as LEDs and solar cells due to the substrate limitation and costs. Hence a bottom-up approach of generating and depositing nanoparticles independent of substrate is required. In this approach, free standing nanoparticles are formed using various procedures discussed next, which can then be deposited on a substrate of choice or to make colloidal solutions.

Deposition methods for free standing nanoparticles

Fabrication of free standing nanoparticles in the liquid phase has been well developed for II-VI (e.g. CdSe, CdS) and IV-VI (e.g. PbS, PbSe) semiconductors [7]. These methods have a high maturity with a good understanding of the kinetics of the reaction and an excellent size control. However liquid phase methods do not translate well to silicon nanocrystals due to the high temperature required for crystallization (e.g. a temperature of 1173 K is required for silicon nanoparticles with a diameter of 8nm [8]). At such high temperatures, the precursor solutions vaporize.

To counter the limitations of liquid phase chemistry, gas phase precursors can be used with the required high temperatures being reached either thermally (pyrolysis) [9] or using a high power laser (photolysis) [10]. However, since the ionized precursors in this case are thermally excited, they coalesce due to frequent collisions (which is governed by their mean free path) leading to a large size variation, with the presence of small nanoparticles to large clusters. This limits the control and tunability of properties. This also necessitate an additional step to separate the nanoparticles on the basis of size adding to

3

system complexity and size [e.g. 11]. Furthermore, a high amount of nanoparticle deposition on the chamber walls is observed in this case reducing the collection rate.

Non-thermal plasma based processes avoid all of the above problems using particle charging, particle confinement, selective nanoparticle heating with the plasma chamber at room temperature which are discussed in the next section.

Non-thermal Plasma based synthesis

Particle growth mechanism

The first reports of nanoparticle formation in plasma chambers came from PECVD experiments using silane as a precursor. There, the nanoparticles were considered as a contaminant and extensive work was done to identify the conditions to reduce the so called "dusty plasma". Bouchoule et al [12-14] did extensive work in the 90's in characterizing such plasma chambers. However it was only after the discovery of high PL from porous silicon that dusty plasma was started to be explored as a source of silicon nanoparticles.

Although the exact growth kinetics of nanoparticles in plasma is dependent on plasma chamber and electrode design, there is some agreement on the basic growth mechanisms involved. Kortshagen [15] and Watanabe [16] give an excellent discussion of the overview of the plasma mechanics. The growth of the nanoparticles occurs through two stages, first a CVD type cluster growth till a size of about 2 nm using a nucleation site; and second a coagulation stage leading to larger particle sizes.

Non-thermal plasma refers to the thermal non-equilibrium among the different species in the plasma. Since the electrons are highly accelerated by the electric field, they have a much higher temperature, sufficient to ionize and dissociate the precursor gas atoms which are initially close to room temperature since they are neutral. This results in ionized free

radicals. These radicals form small clusters of the form Si_nH_m which have a positive electron affinity. Some of these clusters attract electrons to become negatively charged, while others remain neutral. These clusters act as nucleation sites for CVD type growth and increase the cluster size by reacting with either SiH_4, SiH_3 or SiH_2 according to the equation [17]→

$$Si_nH_{2n+1}^- + SiH_4 \rightarrow Si_{n+1}H_{2n+3}^- + H_2 \qquad (1)$$
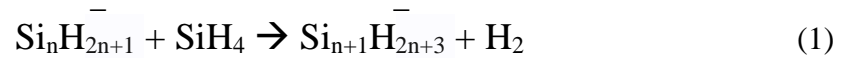
A similar reaction can occur through neutral clusters and which path dominates (whether the neutral or the negatively charged reactions) is determined by the chamber and electrode design.

This growth mechanism continues till the primary particles are about 2nm [12] after which the reaction probability of excited SiH_4 molecules with the cluster decreases leading to no further CVD type growth. At this stage, the plasma contains a high particle density. Due to the large number of particles, there is a mix of neutral and negatively charged particles (because at this stage the particle density is larger than the electron density). These small particles quickly coagglomerate to larger particles, thus reducing the number of particles and ensuring a negative charge on all the particles as shown in figure 2.
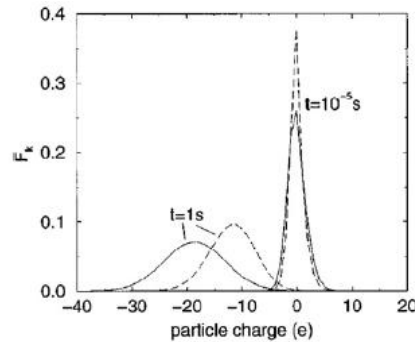
Figure 2 Evolution of particle charge distribution at different times in the plasma. As the time increases, the particle density decreases. At t = 10^{-5}s particle density = 10^{12} cm^{-3} and at t =1s particle density = 3×10^8 cm^{-3}. [15]

This uniform negative charge on the nanoparticles prevents further coagglomeration, leading to a more monodisperse size distribution compared to the gas phase methods.

Further advantage is obtained by the particle confinement. The electrons, owing to their much higher temperatures and mobilities, escape to the chamber walls leading to a high negative charge on the chamber. This leads to an electric potential near the chamber walls called the sheath. This electric field confines the negatively charged particles in the plasma reactor and does not allow the particles to diffuse to the chamber walls (figure 3), preventing chamber deposition and improving collection rates.
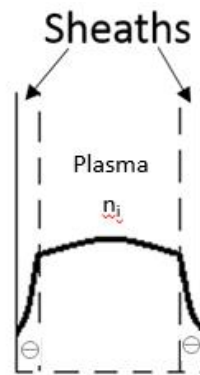
Figure 3 Particle confinement due to negatively charged sheath region

Selective nanoparticle heating

As discussed earlier, an extremely high temperature is required to crystallize the silicon nanoparticles. This requires an excess temperature of hundreds of degrees to be achieved by the nanoparticles since the bulk of the plasma is at room temperature. This is usually achieved by intense heating of the nanoparticles through surface reactions such as electron-ion recombination and Si-H bond formation at the surface. Equation (2) derived by Kortshagen et al [18] using Monte Carlo simulations correlates different parameters of

the nanoparticles in the plasma with the excess temperature under a non-steady state condition.

$$m_p C \frac{dTp}{dt} = \frac{4}{3}\pi R_p^3 \rho C \frac{dTp}{dt} = G - S \tag{2}$$

Here   is the density of silicon, C the specific heat, R_P the radius of the nanoparticle, m_p is the mass of the nanoparticles and T_P the particle temperature as a function of time. G is the heat release term (responsible for raising the temperature of the nanoparticle) and S represents the different heat loss mechanism. The heat loss term is dominated by conduction due to the frequent collisions and quickly dissipates the heat away such that on a macroscopic level, the average excess temperature of the particles is around 100K more than the plasma as shown in figure 4. However, due to the smaller heat capacitance of smaller particles, a large number of spikes in excess temperature are observed in particles undergoing the exothermic reactions (as shown in figure 4) which aid in crystallization. These high temperatures are dissipated quickly by collisions such that the average excess temperatures are lower. This is also reflected by the larger spread of the excess temperature for the smaller nanoparticles in figure 5 which shows that due to their small size, a fraction of small nanoparticles can reach temperatures high enough for crystallization.
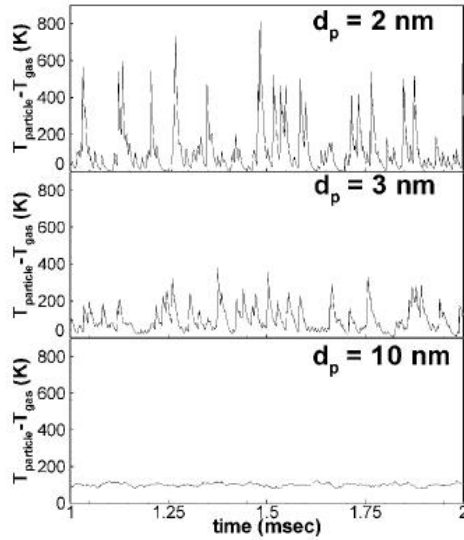
Figure 4 Excess temperature fluctuation of nanoparticles with respect to temperature of the background gas

as a function of time in the plasma. [18]
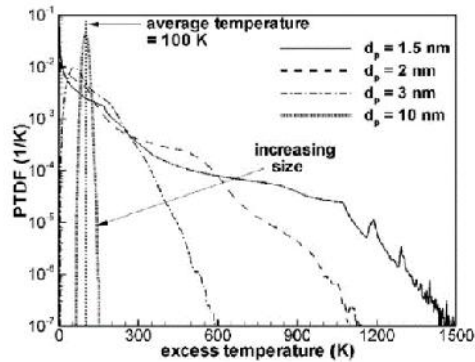
Figure 5 Particle temperature distribution function of silicon nanoparticles as function of size using Monte Carlo calculations [18]

Moreover, the ability of particles in the non-thermal plasmas to have an excess temperature allows us to tune the properties of the nanoparticles over a variety of growth conditions. We can obtain amorphous or crystalline nanoparticles by varying the power, precursor gas flow rates and pressure. The amount of power delivered to the chamber is proportional to the excess temperature while a higher pressure can lead to faster cooling through higher collisions. This is explored in more detail in chapter 4.

The ions and the neutral species generated through the process discussed above constitute the majority of the species in the plasma. Since they are at a relatively low temperature, the average temperature of the chamber wells remains low, negating the requirement for chambers and equipment capable of withstanding high temperatures. This reduces the cost of equipment compared to thermal plasmas or gas phase methods.

Organization of the Thesis

In chapter 2, we explore the aim of the different nanoparticle deposition tools in the Holman lab and report on the development of the analysis tool "Anny".

In chapter 3, the theoretical background and spectrum acquisition methods used for vibrational spectroscopy used in this study are explored, and they are used to characterize Anny against the system parameters (gas flow rates and power) in chapter 4.

Chapter 5 begins with the past work done to understand the origin of PL from c-Si and a-Si nanoparticles, followed by the results from our deposition system.

Chapter 6 presents the future development planned for the tool and the nanoparticles.

Chapter 2

SETUP AND AUTOMATION OF ANALYSIS TOOL "ANNY"
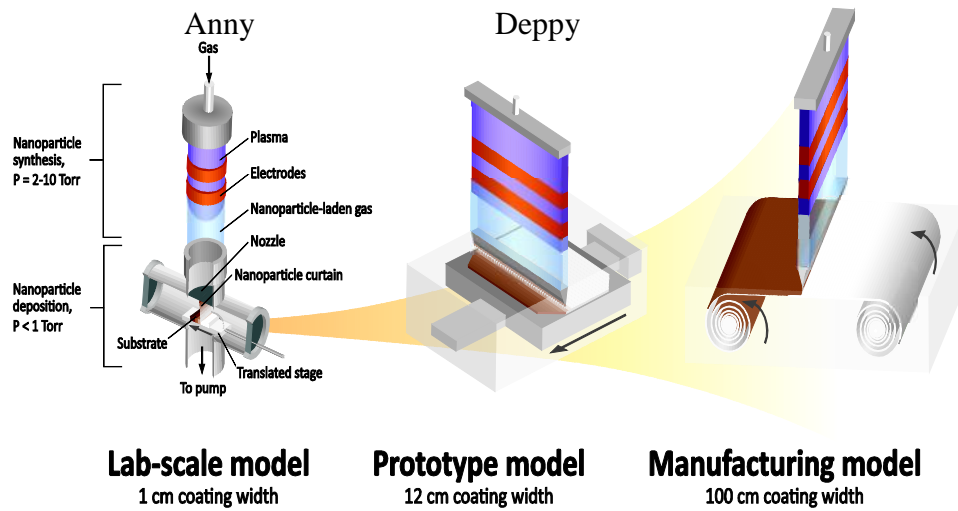
Figure 6 Schematic of Anny and Deppy and how they would enable scaling up to industrial deposition system for silicon nanoparticles

The lab has two novel tools called the Analysis tool "Anny" and Deposition tool "Deppy" to explore the physics behind the growth of silicon nanoparticles and to scale it up to uniformly coat larger wafer areas respectively. This should give us insights into the challenges for scaling up the tools to deposit nanoparticles on tools on an industrial scale as shown in figure 6.
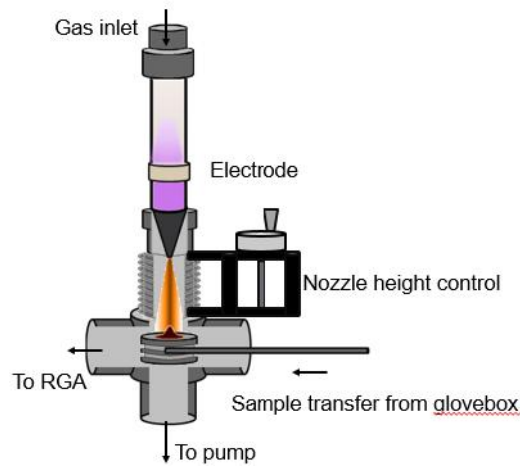
Figure 7 Schematic cross section of Anny

The analysis tool or Anny, is a novel tool designed by Dr. Zachary Holman to enable the analysis of silicon nanoparticles and the plasma using in-situ Fourier Transform Infrared Spectroscopy (FTIR) and Residual Gas Analyzer (RGA) capabilities. The schematic cross section of the tool is shown in figure 7. It contains a 1" diameter quartz tube as the chamber where multiple inductively and capacitively coupled electrode configurations can be tried. The chamber is directly connected to a N_2 glovebox enabling sample transfer for further characterization without exposure to air. A small nozzle at the bottom of the chamber is used to create a choked flow with and the upstream to downstream pressure ratio is kept larger than 30. This accelerates the carrier gases to supersonic speeds in accordance the Venturi effect. The nanoparticles too, by their frequent collisions with the high speed gas molecules are accelerated to supersonic speeds along with the gas and impact the substrate at speeds high enough for adhesion. This decouples the nanoparticle creation and deposition, enabling deposition independent of substrate.

The tool can be broadly classified into two parts –

1. The quartz chamber upstream of the nozzle where a pressure of a few Torrs is maintained for the plasma

2. The section downstream of the nozzle where the pressure can be as low as 10^{-5} Torr using a turbo pump required for the RGA to function

Set-up and automation of Anny

Initially, Anny and Deppy consisted of chambers connected to the glovebox and discrete components such as the 15 solenoid valves for the gases and glovebox door for Deppy, 6 mass flow controllers, pressure sensors, Watlow thermocouple and heater etc.

which were not communicating with each other, and in the case of the solenoids were not even hooked up to the tools. The solenoids are triggered by 24V signals, while the MFCs, Watlow and the motion control used RS-232 for communicating with the computer. The MFCs and the motion control use a standard ASCII code set while the Watlow employs its own communication protocol called ModBus which is communicated through serial communication. The majority of time in 2014 was used in setting up the tool and ensuring the communication between the components using LabVIEW. Towards this aim, National Instruments modules such as the PCIe-8430/8 and the NI 6516 (shown in figure 8) were used to extend the PCIexpress slot in the control desktop to accommodate multiple RS 232 ports and to provide the control signals for the solenoids using NI-DAQ respectively. This setup, with the addition of an external power source with appropriate current rating was used to trigger the solenoids.

(a)   (b)
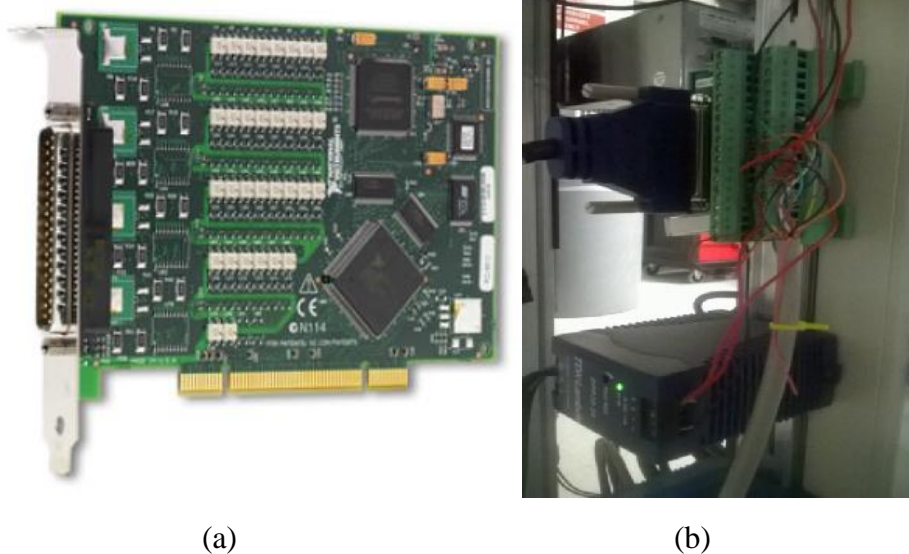
Figure 8 (a)NI 6516 32 channel 30V output PCIe card and (b) the corresponding connections to solenoids and power supply

The MFC flow rates were calibrated to their respective gases using the Horiba

SEC Z500 software. Our silane precursor is a mixture of 95% helium and 5% silane,

while the software only has the capability to use correction factors (CF) corresponding to pure helium. Hence a correction factor has to be multiplied manually for the mixture [19]–

$$CF(5\%SiH4, 95\%He) = \frac{(0.95*CF(He)) + (0.05*CF(SiH4))}{CF(He)} \tag{3}$$

With $CF(SiH_4) = 0.6$ and $CF(He) = 1.45$ [20] which leads to an error of 2.9% in the measured flow rate which has been ignored for now, and the mixture requirement has been reported to Horiba for future software updates.

The LabVIEW code was written to control all the gas valves individually for quick troubleshooting (as shown in figure 9) which was integrated into unified code to enable central control for the tool. The same ideology was approached for the other components, with individual programs for each component which were then integrated into the unified program to make the program modular, and hence easier to debug, and to enable easy troubleshoot of individual components. The algorithm chart for Anny is shown in figure 10 and a similar chart with added complexity due to the higher number of components was used in Deppy. A section of the code used to set temperature for the Watlow thermocouple is shown in figure 11. The unified code for the gas and pressure control in Anny is shown in figure 12.

Figure 9 The LabVIEW code for individual control of solenoid valves for gas flow

Due to the use of silane as a precursor, safety was a big concern and the use of LabVIEW enabled a safer operation of the tool since the number of manual steps was reduced and this also helped in reducing process complexity and deposition time. However some of the steps, such as the sample transfer mechanism and the valve operation for the process pump are still manual and would be automated in future development of the tool.
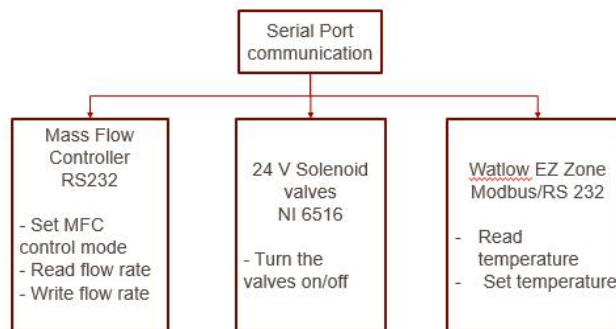
Figure 10 Block diagram for different modules for gas flow control in Anny
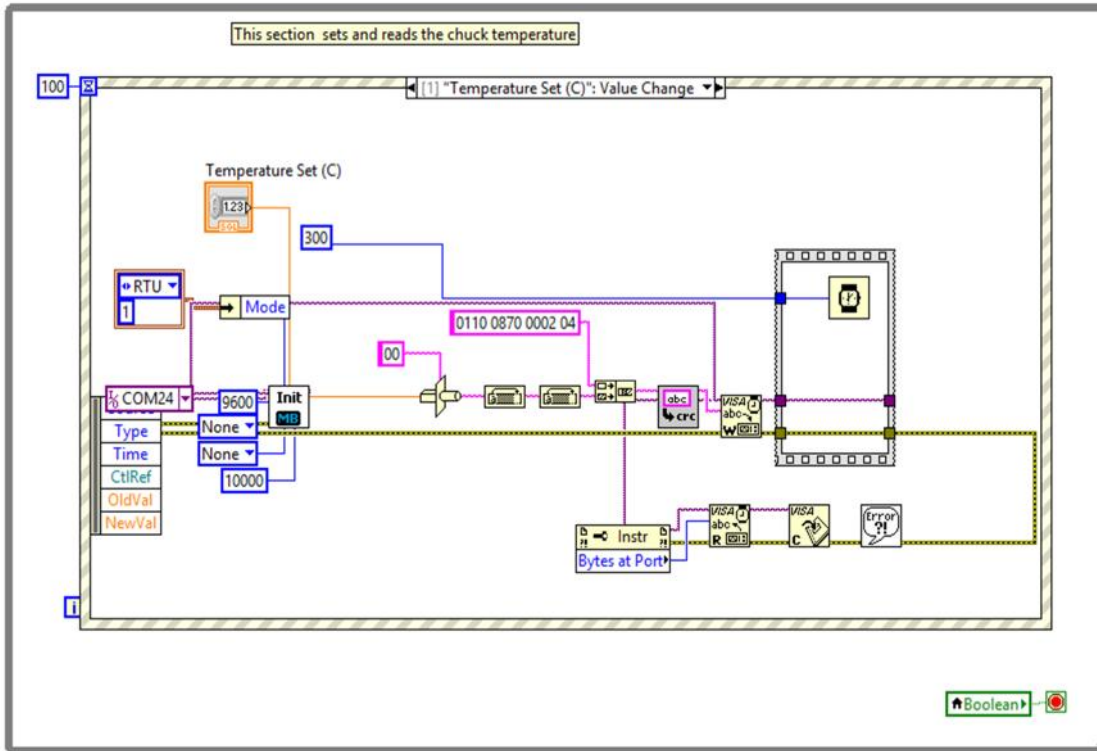
Figure 11 Snippet of the code for setting the temperature for the Watlow
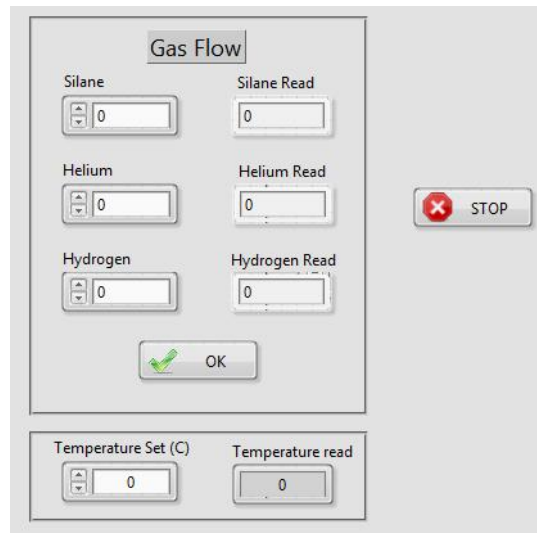
Figure 12 Screenshot of the gas flow control system for the tool

Deposition SOP

Sample Load/Unload

1. Ensure that the valves and MFCs for Anny's precursor gases and the valves connecting the vacuum pumps to the chamber are closed.

2. Vent the chamber to atmospheric pressure using the manual vent.

3. Using the viewport to align, transfer the sample puck to the glovebox transfer arm (y-axis) from the x-axis arm

4. Open the valve connecting the chamber to the glovebox, and extend the y-axis arm into the glovebox.

5. Secure the substrate on the puck using the screws

6. Move the y-axis arm back to Anny

7. Close the valve to the glovebox and ensure the vent valve is closed.

8. Transfer the puck back to the x-axis arm.

   Deposition procedure

1. Switch on the process pump and pump down the chamber by opening the corresponding valve.

2. Set the desired flow rate for silane, hydrogen, helium using the LabVIEW interface and press OK.

3. Wait for 30 seconds for the pressure to stabilize.

4. Switch on the power supply and ramp up the power to the required wattage. (Some impedance match tuning may be required with high H2 dilution)

5. Move the x-transfer arm beneath the nozzle for deposition (x-arm position for the center of the puck to be aligned with the nozzle is 116 mm)

6. Move the arm back to the viewport after the required deposition time.

7. Turn off the power supply

8. Close the MFCs and valves for precursor gases by setting the flow rate to 0 in the LabVIEW interface.

9. Close the valve for the process pump.

Points to note –

1. Ensure that the sample is well secured on the puck.

2. Always leave the chamber under vacuum, close all the valves and turn off the process pump after the experiments are complete.

3. If the puck holder on the y-axis arm is too loose, tighten the screws using the hex key in the glovebox.

Chapter 3

VIBRATIONAL SPECTROSCOPY TECHNIQUES USED IN THE STUDY

In this chapter we would provide an overview of the different characterization techniques used in this study. Specifically, the background of vibrational spectroscopy (Raman spectroscopy and Fourier Transform Infrared Spectroscopy (FTIR)) will be explained with a focus on characterizing the crystallinity, the effect of oxidation on the surface composition and the optical activity of the nanoparticles.

Vibrational spectroscopy

Atoms in a molecule have a certain mass and are connected by bonds which can be viewed classically as a vibrating spring-mass system with the periodic vibrations governed by the masses of atoms, the geometrical arrangement and the strength of the chemical bonds. Each atom has three degrees of freedom (along each Cartesian axis). Hence if there are n atoms in a molecule, the atoms can move in 3n directions (called degree of freedom). However, out of these, three involve translating all the atoms along one of the Cartesian axis, and another three describe rotations. These 6 motions do not change the lengths of the bonds or the angles between them and lead to equivalent systems. Hence there are (3n-6) degrees of freedom and correspondingly (3n-6) normal vibrations in the molecule with bond length displacements of the order of 1-10pm.

Considering diatomic molecules, according to classical mechanics, the vibrational energies are continuous and take the form of a parabola when plotted against the interatomic distance. However, according to quantum mechanics, these energy levels are discrete and for an ideal harmonic oscillator are given by [21]

$$E_i = (v_i + \frac{1}{2}) \, h\nu \qquad (4)$$

18

Where v_i = 0,1,2 are the quantum numbers and v is the vibrational frequency. This ideal harmonic oscillator is shown in figure 13.
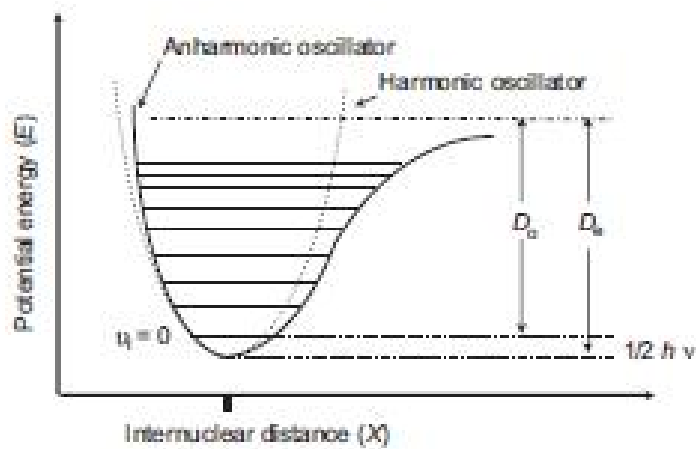
Figure 13 The potential energy diagram comparison of anharmonic and harmonic oscillator [22]

However, real chemical bonds are not harmonic, since change in dipole moment is not linearly proportional to the displacement vector along the internuclear distance axis, i.e. the energy of the bond increases much faster when the bond length is reduced further compared to the minimum energy point. This leads to an anharmonicity as shown with the quantum energy levels no longer split evenly. Here, the case with v_i =0 represents the ground state of the molecule and represents the fundamental vibration of the system. The system can be moved to an excited state by absorbing energy such that $\Delta v_i = \pm$ n where n is an integer. These energy levels are usually in the infrared region (with peaks usually in the 10-4000 cm^{-1} region) and are characteristic for the bond between two atoms. Hence the chemical species can be characterized by monitoring the energy absorbed when the bond is excited.

Two major, complimentary techniques are used to characterize chemical bonds using this method and both of them have been used in this study –

19

1. **Raman spectroscopy** which is useful for characterizing symmetrical bonds

2. **Fourier Transform Infrared Spectroscopy (FTIR)** which is used to characterize non-symmetrical, partially polar bonds

Raman Spectroscopy

When a light quantum with energy $h\nu_0$ (usually from a high stability laser) is incident on a molecule, it can undergo either an elastic or inelastic scattering. In the elastic scattering, called Rayleigh scattering, there is no change in energy of the quanta. During the inelastic scattering process, which has a much lower probability, energy is exchanged with the vibrational energy states leading to an emission of energy $h\nu_0 \pm h\nu_v$ where ν_v is the vibrational energy as shown in figure 14.
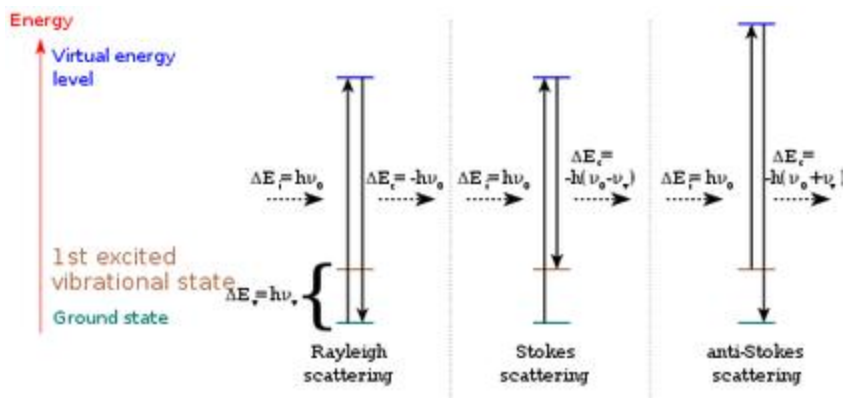
Figure 14 Transitions between ground state and excited state for Rayleigh, Stokes and anti-Stokes scattering [23]

The plus and minus signs refer to whether the vibrational energy is absorbed or emitted and this leads to symmetric peaks on both sides of the Rayleigh scattering peak. According to Boltzmann statistics, since at thermal equilibrium, most of the bonds are at ground state, hence energy is normally absorbed to excite the species to an excited state and Stokes scattering has a much higher probability (and hence a higher signal to noise

ratio than the anti-Stokes scattering) and hence it is generally used for characterization. Since the energy of the vibration is characterized by the change in the energy of the input photons, hence the spectrum is plotted in terms of shift of energy from the input photon energy, or the Raman shift.

As discussed earlier, since Raman spectroscopy is used to characterize symmetrical bonds, it provides a very convenient method to characterize Si-Si bonds in crystalline/amorphous silicon which is the application of interest in the current work.

Spectrum acquisition

The measurements were done using the Renishaw system in the Defect Lab. with a 532nm laser, a Si CCD camera and 2400 lines/mm grating. Spectrum acquisition with Raman is a practice in optimization of signal to noise ratio and acquisition times while ensuring no damage to the samples. The main parameters to control the quality of the spectrum are laser power and the acquisition time.

Laser power is the most important factor in the determination of a good signal. The laser used in the studies has a 100mW output. A 50x lens with a numerical aperture of 0.5 is used, which leads to a laser spot diameter 1.298μm. This means that the power density of the laser operating at full power is $7.56 \times 10^6 W/cm^2$. Although a higher incident laser power ensures a higher signal to noise ratio, however the nanoparticles are especially prone to damage from the laser, with crystallization of amorphous nanoparticles observed at power densities as low as 0.5% ($3.78 \times 10^4 W/cm^2$) as shown in figure 15(a). As can be seen from the figure, a power of $3.78 \times 10^4 W/cm^2$ and above shifts the spectra towards the right which is due to crystallization and is observable in multiple samples. A power of

$3.78 \times 10^3 \text{W/cm}^2$ has a lower signal to noise ratio. Hence a power of $7.56 \times 10^3 \text{W/cm}^2$ is optimum.

(a)   (b)
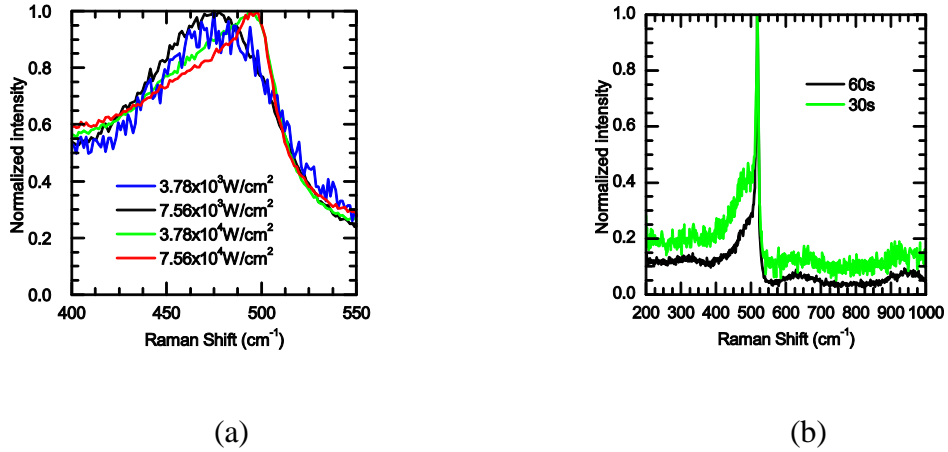
Figure 15 Dependence of Raman peak position and signal to noise ratio on (a) laser power, (b) acquisition time

Similar studies on acquisition times shown in figure 15(b) shows that an acquisition time of 60s shows the improvement in signal to noise ratio from 30s but any further increase does not improve the spectrum much. Hence all the Raman measurements in this work were performed at $7.56 \times 10^3 \text{W/cm}^2$ power density and 60s acquisition time. Another important thing to remember is to ensure that the spectrum at 0 cm^{-1} Raman Shift is not collected by modifying the collection range accordingly as that might lead to collection of the Rayleigh spectrum which would dominate the spectrum.

Crystallinity calculation from Raman spectrum

As discussed earlier, Raman spectroscopy is excellent for characterizing symmetric bonds such as Si-Si bonds. Studies from bulk silicon have shown that a-Si has a broad peak centered at 475 cm^{-1}, microcrystalline silicon has a peak around 510cm^{-1}, and crystalline silicon has a strong, narrow peak at 520cm^{-1}.

However, in silicon nanoparticles these peak positions change a little due to the strain in the structure because of the small size. This is especially evident in the crystalline peak, with the peak shifting to smaller wavenumbers by as much as 6cm^{-1} for particles 2nm in size. This is sometimes being used to characterize the size [24].

To find the amount of crystallinity in the nanoparticles, a 3 peak Gaussian fit for the 3 peaks described above is used with the peak positions varying within $\pm$ 3 cm^{-1} to account for the effect of size in the structure, which gives a rather unique fit. The percentage of crystallinity is then determined from the areas of the peaks using

$$\text{Crystallinity (\%)} = \frac{Area_{520} + Area_{510}}{Total \ area \ under \ the \ curve} \times 100 \tag{5}$$

Where Area$_{520}$ is the area under the peak due to crystalline silicon at 520cm^{-1} and Area$_{510}$ is the area under microcrystalline silicon at 510cm^{-1}

Any peak fit software maybe used for this purpose. In this work, peak analyzer template from OriginPro was used due to the ease and batch processing capabilities of Origin. A sample for the peak fit is shown in figure 16.
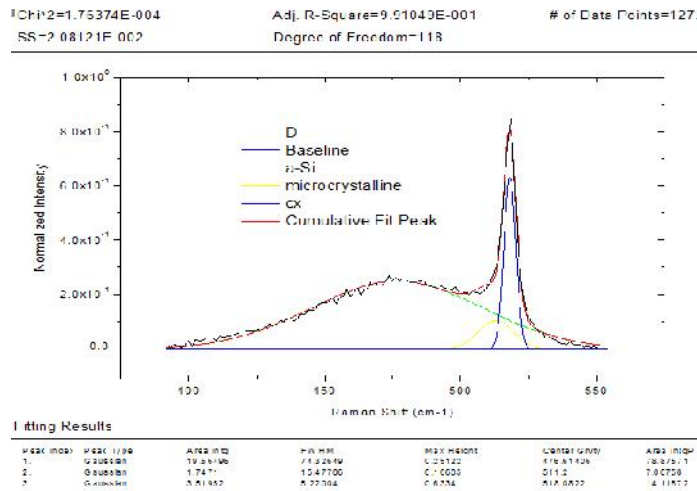
Figure 16 3 peak fit for a partially crystalline nanoparticle sample.

23

Infrared Spectroscopy

Infrared spectra generally measure the transmittance of light quanta through the sample. This technique is useful for identifying polar, non-symmetric bond vibration modes such as Si-H, Si-O, Si-O-H, etc. Typically the light source is broad band and emits in a large range of frequencies of interest such as mid-IR region. The transmitted light directly excites the molecules to excited states and has absorption bands whose frequencies are proportional to the energy difference between the vibrational ground and excited states. The absorbed (or transmitted) light can be directly related to the concentration of the material under test by using the Lambert-Beer law. The spectrum is obtained by plotting the absorbance vs the wavenumber.

FTIR vs Dispersive IR

Traditionally, an IR spectrometer was dispersive, which consisted of a radiation source which emitted a broadband source of IR light, a monochromator and a detector. The incident light is essentially split into 2 beams, with one being used for reference, and the other passing through the sample, which would be absorbed and give the required spectrum. After the incident radiation has travelled through the sample, it passes through a monochromator where it is split into its constituent frequencies and only a specific wavelength passes forward using a grating and slit mechanism. The incident light is then detected by the detector which converts the optical signal to electrical signal which is compared with the reference wavelength and any differences in the intensity in a group of wavelengths are detected. The schematic of the setup is given in figure 17. Since small

groups or wavelengths are compared one at a time, this is a slow process, especially for high resolutions and has a low sensitivity.
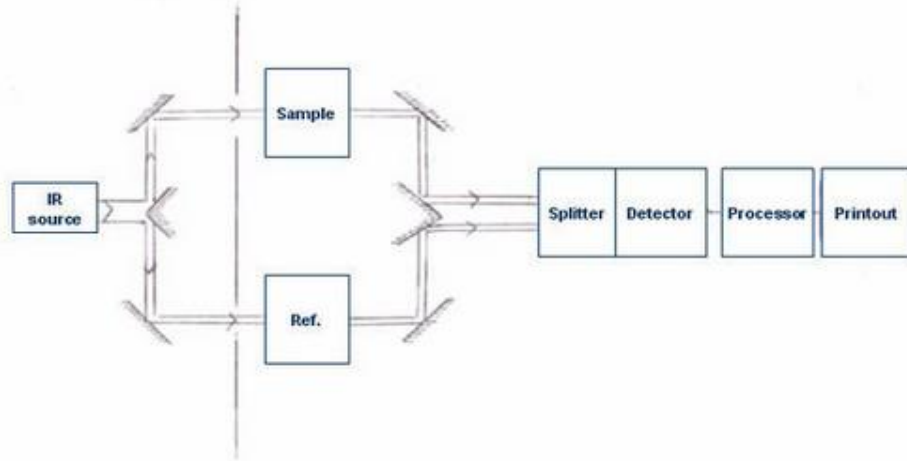
Figure 17 Schematic of a dispersive IR system [25]

FTIR, in contrast, has a higher scan speed, better sensitivity, a greater optical throughput and is simple with just one moving part. An FTIR uses an interferometer instead of a monochromator and can scan multiple frequencies simultaneously.

Interferometers consist of a beamsplitter which divides the incident beam into two parts, one goes to a fixed flat mirror while the other one goes to a mobile one. These two parts are reflected back and interfere with each other due to the different path lengths, and hence different phases. This leads to an interferogram as shown in the figure 18 which is a waveform limited in the time domain but correspondingly has information about every IR frequency emitted from the source, and can be transformed to frequency domain using a Fourier Transform.

Transmission/ absorption studies for FTIR normally require very thin films or colloidal solutions due to the high absorbance which require complex sample preparation. Hence a reflection based system is used in the lab, which is discussed briefly next.
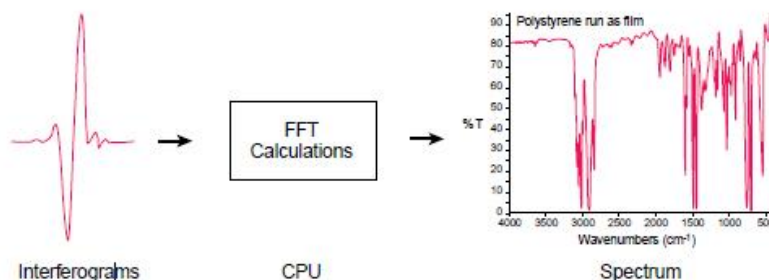
Figure 18 Interferogram from a FTIR in the time domain and its FT to frequency domain spectrum [26]

Spectrum acquisition

The measurements are taken using the Perkin Elmer setup in our lab. Since the samples from Anny are in the form of powder, we use a diffuse reflectance (DRIFTS) accessory for the measurements. The rough, irregular surface of the powder leads to multiple reflections instead of a single specular reflection. Since this is a non-contact measurement technique, no elaborate sample prep is required.

(a)   (b)

Figure 19 (a) Schematic of DRIFTS accessory, (b) Schematic of diffuse reflectance from a powder [27]

Since the amount of material deposited in Anny is too small to cover the puck supplied with the DRIFTS accessory, the measurements are made directly on the substrate by removing the front plate of the DRIFTS accessory and placing the substrate directly on

the sample holder. The monitor function of the software is now used to align the substrate properly, since the notch alignment is not accurate in our case.

Steps for measurement and data analysis –

1. Remove the front plate

2. Run the background measurement

3. Run the monitor, and adjust the sample holder arm until your sample is in the correct location (for the samples from Anny, this corresponds to the situation when the difference from maximum signal of the substrate is the highest because this represents the location with the most sample. This is shown in figure 20)
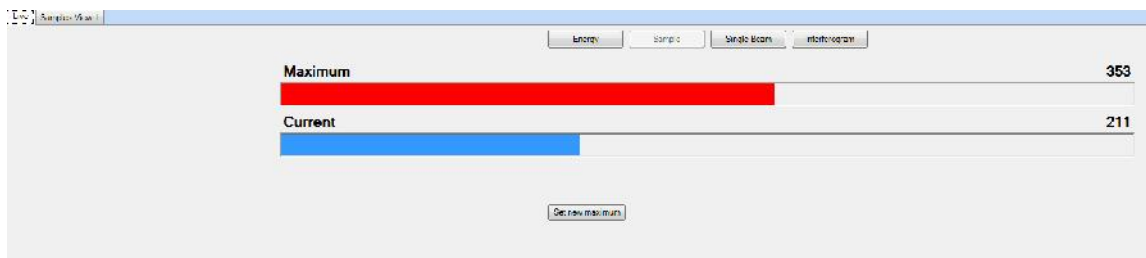
Figure 20 Monitor function from the FTIR where the 'maximum' signal is from the substrate and the dip is due to the sample.

4. Halt the monitor, set the required wavenumber range for the spectrum acquisition and run.

5. After, the spectrum has been acquired, convert the spectrum to absorbance (it is set to the transmittance by default) using the process tab.

6. Run data tune-up on the spectrum, which corrects the baseline and removes some random noise and use other operations as required.

Calculation of hydrogen passivation stability

Chemical bonds in FTIR spectrum have absorption bands at different locations either due to different vibration mechanism (e.g. changes in bond length vs changes in bond angle in $Si-H_x$ have different peak positions) and different backbondings (such as Si-O-Si or $Si(OH)_x$). Since the absolute signal intensities are dependent on the amount of sample, for this study the evolution of intensity Si-O-Si peak around 1070 cm^{-1} over a week is normalized to the initial $Si-H_x$ peak intensity at 2000-2200 cm^{-1}. These peaks are chosen since they reflect peaks due to single species with little overlap from other species, reducing errors. Again, the peak analyzer template in OriginPro is used for the waveform modification, baseline subtraction and evaluation of the peak areas.

Chapter 4

CHARACTERIZATION OF TOOL PERFORMANCE– EFFECT OF GAS FLOW RATE AND POWER ON CRYSTALLINITY AND DEPOSITION RATE

The main variables to be controlled in this study were the chamber conditions and the distance between the nozzle and the substrate. The distance controls the density, thickness and area of deposition as shown qualitatively in figure. A deposition height of 1.7cm was chosen for all depositions.

Figure 21 Effect of increasing the distance between the nozzle and the substrate on the deposition profile. The distance is increasing from 0.7cm to 3.2cm, going from 1 to 5.

The chamber pressure varies linearly with the gas flow rates. Hence, the pressure ratio upstream of the nozzle to downstream changes from 30 to 100 depending on the gas flow, enabling substrate independent deposition in excess of sonic speeds as demonstrated by similar properties of depositions on glass, gold coated silicon and TEM grids for Raman and PL, FTIR and TEM studies respectively.

Crystallinity is one of the most important properties governing the PL with multiple groups identifying crystalline particles as having a much higher quantum yield and PL peak tunability. Hence a major aim of this study was to identify the conditions for the growth of highly crystalline particles with high deposition rates.

The crystallinity and surface passivation of the nanoparticles is dependent on the chamber conditions i.e. the power supplied to the electrodes, helium dilution and the silane flow rate. The effect of each of these on crystallinity is characterized using Raman spectroscopy, while the deposition rate is characterized qualitatively. The deposition times for all the experiments is kept constant at 1 minute.

Effect of helium dilution

For this set of experiments, the SiH_4 flow rate was kept constant at 6 sccms, and the Helium flow rate was gradually increased in intervals of 2 sccms at constant power of 100W as shown in table 1.

Table 1 Run conditions to study the effect of helium flow rate on crystallinity of nanoparticles

Run #	1	2	3	4	5	6	7	8	9
SiH4 (sccm)	6	6	6	6	6	6	6	6	6
He (sccm)	2	4	6	8	10	12	14	16	18
Power (W)	100	100	100	100	100	100	100	100	100
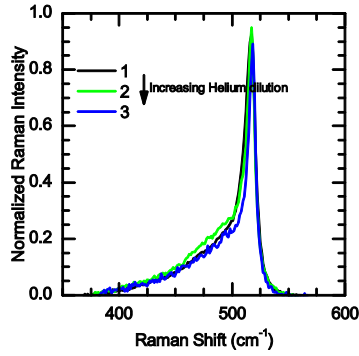
(a)
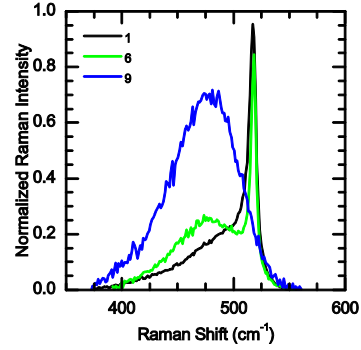
(b)
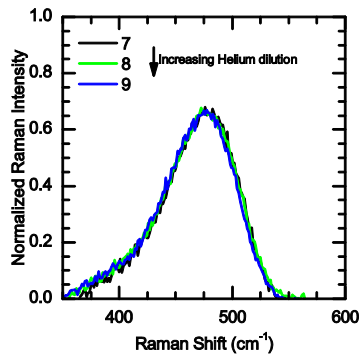
(c)
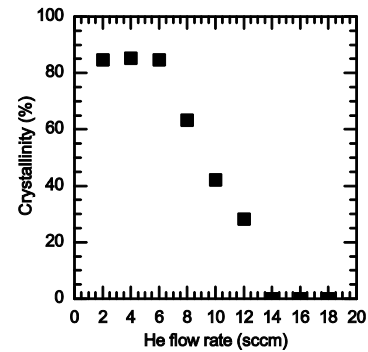
(d)

Figure 22 Effect of helium flow rate on the crystallinity of silicon nanoparticles (a) the spectra of highly crystalline nanoparticles, (b) the increasing peak at 480 cm-1 with decreasing crystallinity, (c) the spectra of highly amorphous nanoparticles, (d) the net effect of Helium flow rate on crystallinity

We see from figure 22(a) that at low Helium concentration we get highly crystalline nanoparticles with crystallinities saturating around 85% (calculated using a 3 peak fit). The high crystallinities can also be confirmed from the lattice fringes observed in corresponding TEM images as shown in figure 23. On increasing the dilution rates, the crystallinities remain constant for a while and then start dropping as shown in fig 22(b) and eventually only amorphous nanoparticles are obtained as observed from fig 22(c) and a further increase of dilution has no effect.

The saturation of the maximum crystallinities of the nanoparticles at ~85% has been reported by other groups and might be due to amorphous type layer at the surface of the nanoparticles due to the high curvature of the spherical nanoparticles and the termination of the continuity from the bulk.
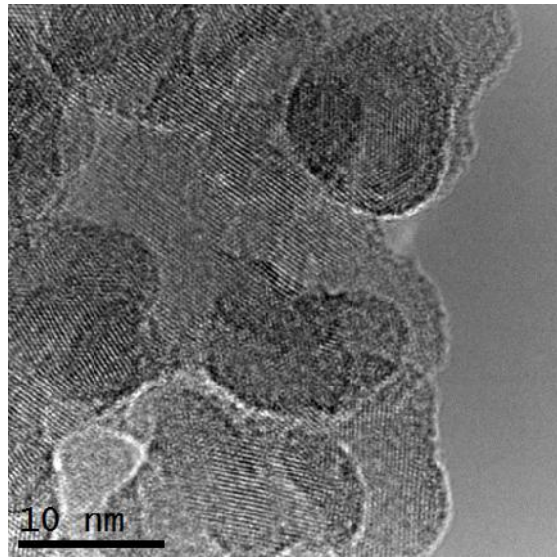
Figure 23 TEM image for highly crystalline nanoparticles corresponding to run 1 showing lattice fringes, confirming high crystallinity.
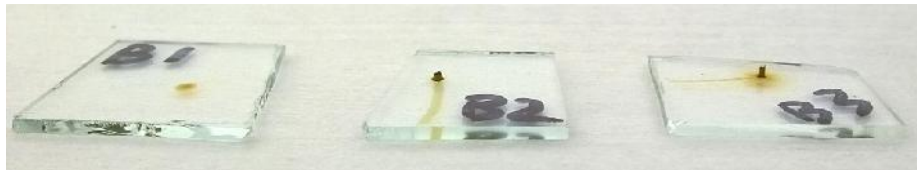
Figure 24 Increasing deposition rate with increasing Helium flow rate for 3 crystalline samples (B1 has the lowest dilution while B3 has the highest)

Moreover, deposition rate was found to increase with the Helium dilution (as shown in figure 24).

Effect of power

For these experiments, the flow rates were kept constant at 6 sccm of SiH_4 and 10 sccm of He. We chose this flow rate since the nanoparticles at these flow rates were partially crystalline at 100 W and would give us the entire spread of crystallinities on moving from 75 W to 150 W as shown in Table 2.

Table 2 Run conditions to study the effect of power on crystallinity of nanoparticles

Run #	1	2	3	4
SiH4 (sccm)	6	6	6	6
He (sccm)	10	10	10	10
Power (W)	75	100	125	150
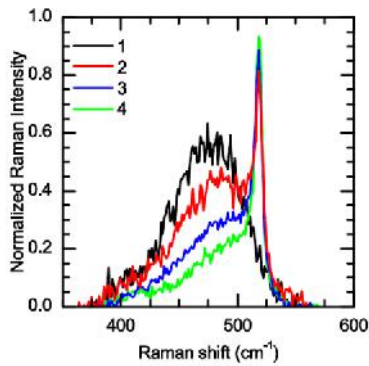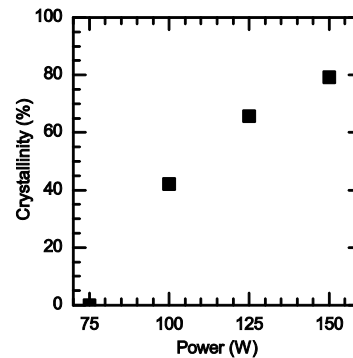
(a)   (b)

Figure 25 Effect of power on the crystallinity of silicon nanoparticles (a) the increasing peak at 480 cm-1 with decreasing power, (b) the net effect of power on crystallinity

We find that the crystallinity increases with power (as shown in figure 25). Also, the deposition rate decreases on going from a-Si to c-Si i.e. on increasing the power.

Effect of Silane flow rate

For these experiments, we kept the ratio of SiH_4 to He and the power constant and increased the flow rate of the SiH_4 by 2sccms.

Table 3 Run conditions to study the effect of silane flow rate on crystallinity of nanoparticles

Run #	1	2	3	4
SiH$_4$ (sccm)	8	10	12	14
He (sccm)	0	0	0	0
Power (W)	100	100	100	100
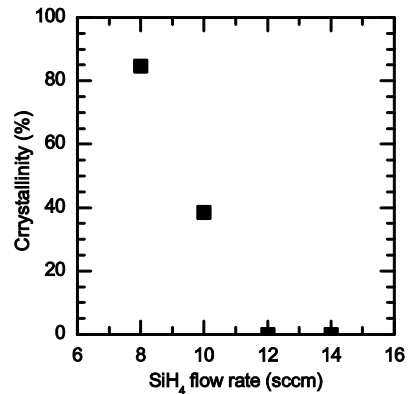
Figure 26 The effect of increasing silane flow rate on crystallinity

Once again, we observe the crystallinities decreasing with increasing flow rates with a maximum crystallinity of about 85% as shown in figure 26. We also observe that the deposition rate increases with silane flow rate due to an increase in pressure ratio across the nozzle and an increased amount of precursor.

This leads us to conclude that the quantity governing the crystallinity is power density (power to precursor gas ratio) since a high energy is required to dissociate the SiH$_4$ molecules and ionize the He atoms.

Discussion

The increasing crystallinity and decreasing deposition rate with decrease in gas flow rates and increase in power can be explained by considering a model consisting of 3 threshold power densities (described in order of increasing power densities):

34

1. Power for dissociation (P_{dis}) which is the minimum power required to dissociate silane to active radicals (SiH_2 and SiH_3 which are necessary for particle growth).

2. Power for crystallization (P_{cr}) which is the minimum power at which a fraction of particles large enough for detection obtains enough excess temperature to crystallize.

3. Power for rupture (P_{rup}) which is the minimum power at which the nucleation sites (clusters of the form Si_nH_m described earlier) break apart reducing the nanoparticle growth. This is confirmed by the observance of decreasing deposition rates at high power levels.

As we decrease the gas flow rates or increase the power, the power density increases from P_{dis} to $P_{rup.}$ Starting with P_{dis}, as the power density is increased, due to Boltzman statistics, the number of particles/clusters with energies large enough to crystallize and rupture increase. This leads to an increase in crystallinity and a decrease in deposition rate. Once, the power density is high enough for the maximum crystallinity to be observed, further decrease in dilution increases the rate of rupture leading to a decrease in deposition rates. This is shown in figure 23 for three crystalline nanoparticle depositions.

Chamber deposition at high power and high silane flow rate

We also tried a high SiH_4 flow (30-40 sccm) and high power (150-200W) to confirm the hypothesis of the importance of power to silane ratio. The crystallinities and optical performance of the nanoparticles in this case followed similar trend compared to the nanoparticles obtained at lower silane flow rates and power. Also, a higher deposition rate was observed owing to the high precursor flow rate.

However, in this case a high amount of deposition on the chamber walls was observed (as shown in figure 27) which can lead to eventual drifts in the characteristics of the nanoparticles deposited under same conditions leading to instabilities in the system performance. This behavior at large silane flow rate can be attributed to higher particle density and higher particle energies which lead to more particles under the Boltzmann-Maxwell distribution obtaining enough thermal energy to overcome the electrostatic barrier of the plasma sheath discussed in chapter 1. This explanation assumes that the electric field in the sheath stays constant with changes in pressure and further measurements are required to prove this assumption.
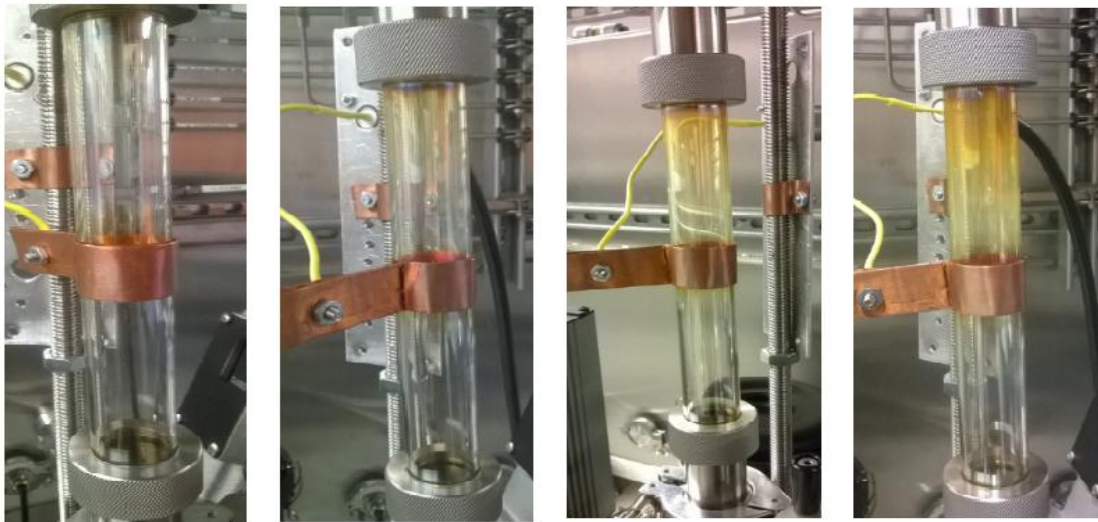
Figure 27 Images showing the increased deposition on the chamber on successive depositions at high power, high silane conditions

Moreover, the plasma at high power was visibly less stable and twitchier which might lead to non-repeatable results. The chamber also heated significantly ($87^{O}C$ after a 1 minute deposition at 170 W) which leads to further instabilities and would require active cooling for long deposition runs.

This, along with the lack of high deposition rates required for Anny, suggests that we should use lower silane flow rate, lower power conditions for growth in Anny.

In the next section we discuss the PL response from nanoparticles and the effect of surface properties on the PL.

Chapter 5

PL FROM AMORPHOUS AND CRYSTALLINE NANOPARTICLES

In this chapter, we would first discuss the theoretical background and past work done on the study of PL from silicon nanoparticles. We discuss the differences in origin from amorphous and crystalline nanoparticles. Then we present some experimental results from Anny and discuss the implications of these results on the responsible PL mechanism.

Origin of PL from C-Si silicon nanoparticles

In spite of the almost two decade long research, there is still some uncertainty regarding the reasons behind the high photoluminescence from silicon nanocrystals. A major reason for that is the complex interplay of the various factors involved, i.e. the size of the nanocrystals (which affects the quantum confinement), their crystallinity, the surface defect states (which lead to radiative or non-radiative recombination pathways depending on the surface passivation), the surrounding (SiOx/SiNx matrix or free standing nanoparticles) and inter nanoparticle interaction.

The optical response of any semiconductor is based on two competing factors (radiative and non-radiative recombination) which are characterized by their respective lifetimes.

$$\eta = \frac{\tau_R^{-1}}{\tau_R^{-1}+\tau_{NR}^{-1}} = \frac{\tau_{NR}}{\tau_R+\tau_{NR}} = \frac{\tau}{\tau_R} \tag{6}$$

Where η is the efficiency of radiative recombination and τ_R and τ_{NR} are the radiative and non-radiative recombination lifetimes respectively.

According to the prevalent theory, the high PL from crystalline nanoparticles can be explained with the interplay of 2 factors:

(1) Enhanced radiative recombination from the core of the nanocrystal due to quantum confinement (in nanocrystals) and spatial confinement in amorphous nanoparticles

(2) The effect of radiative/non-radiative surface states which become even more important due to the high surface to volume ratio in nanoparticles.

Quantum Confinement

The energy bands in bulk semiconductors are formed due to changes in atomic energy levels due to the nearest neighbor interaction, with the width of the bands governed by the strength of interaction (i.e. stronger bonding leads to larger bands). The bands are centered on the energy levels, developing near the center first and then moving towards the edges. Since the Fermi level in semiconductors lies in between two energy levels, edges of the band dominate low energy optical behavior. As the dimensions of the semiconductors reduce from the bulk to the nanometer regime (especially lower than the Bohr radius) as shown in figure 28, the edges of the conduction and valence bands split into discrete states which gradually moves towards the center, hence increasing the bandgap, leading to a blue shift of PL peak with decreasing size.
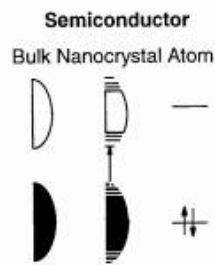
Fig.28 Evolution of density of states with decreasing dimensionality of semiconductor. Fermi level lies between the conduction and valence bands. The density of states becomes discrete on the edges and the bandgap increases with decreasing size. [28]

The mathematical expression for the radius dependency of the change in band gap in spherical nanocrystal in given by [29]→

$$E_g^{NC}(R) = E_g + \frac{h^2}{8R^2}\left(\frac{1}{m_e} + \frac{1}{m_h}\right) - \frac{1.8e^2}{\varepsilon R} \tag{7}$$

Where E_g^{NC} is the bandgap of the nanocrystal, R is the radius of the nanoparticle, Eg is the bandgap of the bulk, m_e and m_h are the effective masses of electrons and holes, is the dielectric constant of the nanocrystal, and e is charge of electron. The 2nd term in this equation represents the quantum confinement and the third term represents the Coulomb interaction between electrons-hole pairs [30]. Both increase with decreasing sizes. At sizes less than the Bohr radius, the 2nd term (due to quantum confinement) dominates the equation due to its inverse square relationship which leads to an increase in bandgap with decreasing size.

Although this equation was derived for direct band gap semiconductors, it is a good approximation for silicon nanoparticles.

The quantum confinement from the core of nanoparticles has also been explained more quantitatively by the numerous theoretical electronic band structure calculations using tight binding model [31,32] and empirical pseudopotential method (EPM) [33,34] methods. Barbagiovanni et al provide a nice comparison of the different theoretical methods used to analyze the band structures of silicon nanostructures [35] which only goes to confirm that although the quantum confinement is very well understood in isolation at a physical level, its interaction with other factors in a real system are not well modelled.

The increased PL quantum yield from nanoparticles is usually attributed to increased oscillator strength which leads to a higher emission efficiency. The oscillator strength is a function of the momentum transfer or coupling efficiency between initial and final states. This is governed by the overlap between electron and hole wave functions which increases with decreasing dimensionality as shown in figure 29[35]
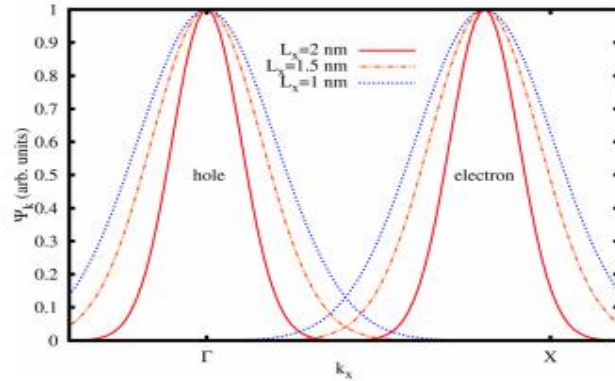
Figure 29 Plot of a Gaussian envelope function for a single confinement direction in k-space [35]

Theoretical calculations based on the theory above have been done on c-Si nanoparticles. A good match between theory and experiments, especially the increasing blue shift and increasing quantum yield have been confirmed by several groups as shown in figure 30. Similar results are also obtained in our experiments.

(a) (b)
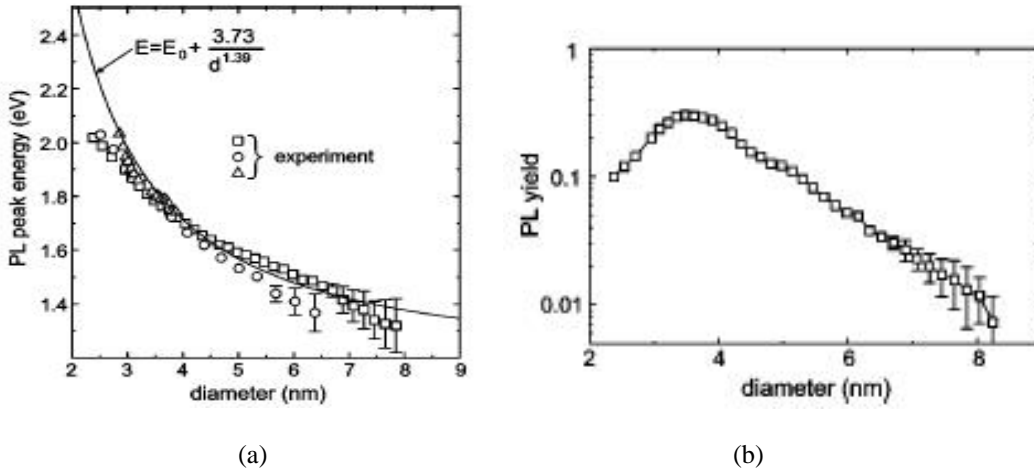
Figure 30 (a) Correlation between average diameter and PL peak energy. Solid curve represents the theory and the data points are form silicon nanoparticles formed by pyrolysis of silane by pulsed CO_2 laser. (b) Measured PL yield as a function of the diameter of the particles. The decrease in QY for particles smaller than 4nm might be due to reduced passivation because of the high surface curvature [36]

The bandgap has also been proposed to be indirect for particles above 4nm with phonon assisted transitions dominating the radiative recombination. For indirect bandgap materials, the absorption is given by –

$$\alpha(h\omega) \propto \omega^{-1}(h\omega - E_g)^2 \tag{8}$$

41

Hence the linear behavior in the absorption spectrum of the silicon nanoparticles as shown in figure 31 provides proof for indirect bandgap.
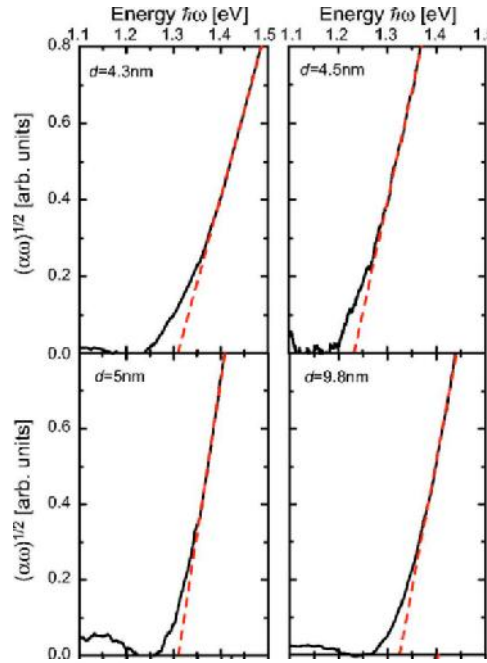
Figure 31 Absorption data for silicon nanoparticles with diameters between d=4.3 nm and 19.2 nm, plotted as $(\alpha\omega)^{1/2}(\frac{\hbar\omega}{2\pi})$ corresponding to an indirect semiconductor [37].

Due to the indirect bandgap, the radiative recombination lifetimes, although much lower than bulk silicon, are still higher than direct bandgap (e.g. II-VI) nanoparticles [39]. This makes the passivation of surface states in silicon nanoparticles more important.

Effect of surface state passivation
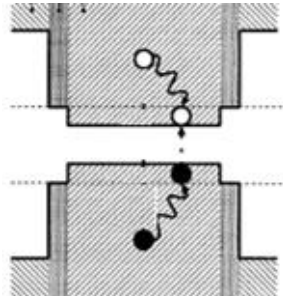
Figure 32 The electronic band structure of silicon nanoparticles passivated by higher bandgap hydride with an intermediate interface region. The image shows electron hole pair generation at the core, which quickly thermalizes to the band edges and is confined leading to radiative recombination from the core [38]

Surface state passivation refers to encasing the core of the nanoparticles with a material with a larger bandgap with an atomically abrupt jump as shown in the figure 32. In such a scenario, the electron hole pairs generated in the core of the nanoparticle quickly thermalize to the lowest core state where they are confined and recombine radiatively. This also keeps the PL peak narrow as long as size homogeneity is maintained. The most important criteria of the effectivity of a surface passivation is that it should not lead to the introduction of mid-bandgap energy levels.

As discussed above, a large variety of theoretical calculations for the quantum confinement are available, but most of them assume hydrogen passivation due to its simplicity. Theoretical calculations based on passivation by oxygen or organics is lacking and the experimental data suggests contradictory effects of hydrogen or oxygen passivation on the PL yield and peak position depending on the growth conditions and the matrix surrounding the nanoparticles. Also the studies on stability of hydrogen passivation are contradictory with respect to the PL evolution with oxidation.

Oxygen is usually attributed to a blue shift in the PL although the mechanism is still under debate. [40] report a smooth blue shift in PL peak energy which is attributed to a decreasing core size with oxidation leading to a higher quantum confinement. This is further supported by evidence of decreasing core size by successive HNO_3 and HF etches by Swihart et al [41], where they oxidixe the nanoparticles and etch the oxide, reducing size and blue shifting the peak.

[40] also report an increasing PL intensity with oxide passivation attributed to increase in intensity due to quantum confinement.

Other groups have reported a superior passivation with hydrogen with the PL decreasing on exposure to air [42-44] (as shown in figure 33) or upon exposure to high temperature [45] or UV light [46]. This is further supported by electron spin resonance measurements which show an increase in non-radiative recombination centers (dangling bonds) upon oxidation of the hydrogen passivate surface leading to a decrease in quantum yield [47, 48]. These reports are similar to our findings and underline the importance of characterizing the method of growth since different growth conditions lead to different hydride/oxide species (as is shown by the difference in optical response of Si-O-Si vs Si=O termination [49,50]) at the surface modifying the optical characteristics.
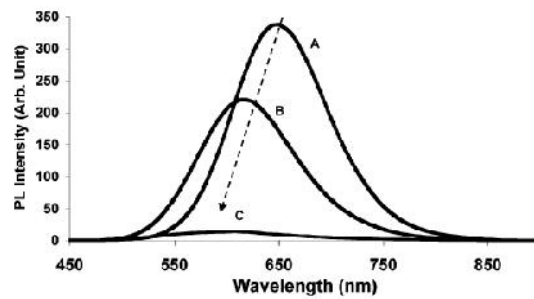
Figure 33 Instability of PL spectrum upon exposure to air for nanoparticles passivated by Hydrogen. Spectrum A, B and C are for samples immediately after production, after 1 day and after 12 days respectively [42]

Origin of photoluminescence from a-Si nanoparticles

PL from bulk a-Si

Like crystalline silicon, a-Si still maintains short range order (like the tetravalency of silicon along with the bond angles, bond lengths etc.) due to the covalent nature of the bonds. The bulk band gap, which is formed by the splitting of the electron duplet in a covalent bond and is strongly determined by the short range order (as proved by tight binding simulations [51]), remains similar in crystalline and amorphous silicon. However, the lack of a long range order distinguishes it from crystalline silicon since the lack of

44

periodicity means that the electron and hole wave functions are no longer delocalized in space (according to Bloch's theorem), but are localized due to the disorder instead. The structural disorder introduces localized band tail states due to the bond length/bond angle variations and mid gap states due to structural defects (the chief being the dangling bonds from silicon) leading to a band structure as shown in figure 34. As can be seen, the abrupt band gaps of crystalline silicon are replaced by the broadened band tail. This long range disorder leads to the loss of k-conservations rule, and reduces the carrier mobility (because of frequent scattering), hence fundamentally changes the recombination mechanisms in a-Si. This leads to the observance of a high quantum yield, broad peak at low temperatures, which is quenched at room temperatures as discussed later in the chapter. It can also be seen from the figure 34 the density of states deep in the band tail (due to highly localized states) is lower than the shallow states which would have a major impact on spatial confinement in a-Si:H nanoparticles discussed later in the chapter.
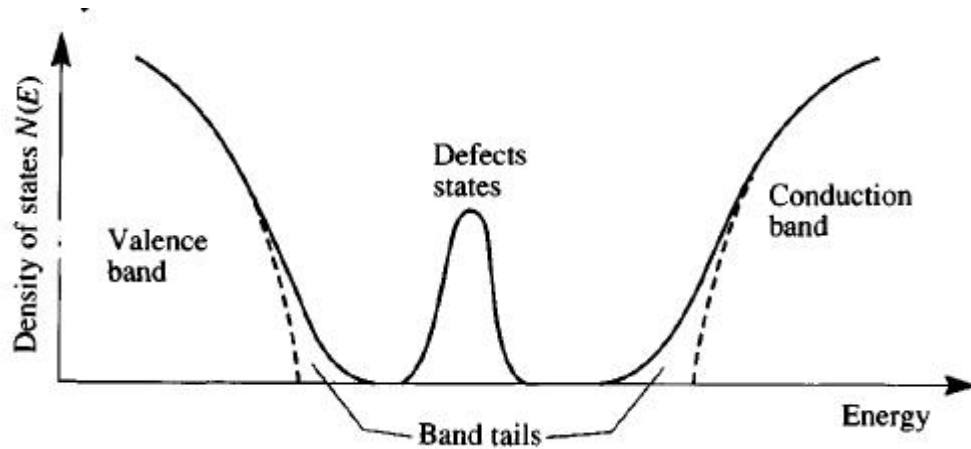
Figure 34 Band structure of bulk a-Si [52]

Illumination of a-Si:H leads to the generation of excess electron hole pairs which populate the extended and localized states at the band edges. As can be seen from figure 35, the recombination process in a-Si:H is dominated by two steps. First, an excited

electron or hole first loses energy by thermalization within the band and the band tails, eventually reaching the lowest energy levels in the band. Then, the electron-hole pair recombines either by radiative or non-radiative recombination with the release of a photon or phonon respectively. The thermalization andd radiative recombination mechanisms are discussed next.
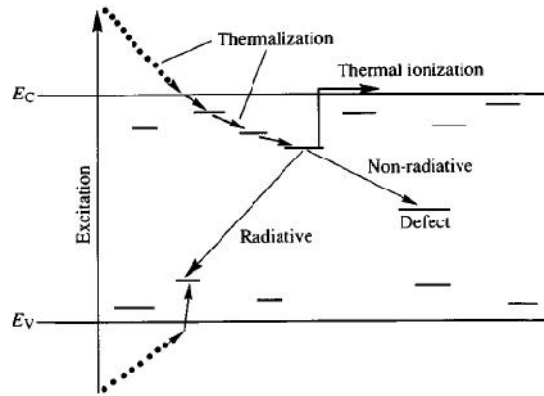
Figure 35 Energy loss mechanisms for generated electron hole pairs in bulk a-Si [52]

Radiative Recombination

a-Si:H shows a larger than 30% quantum yield at temperatures less than 50 K. The large density of band tail localized states in a-Si is the most important factor in the recombination mechanism. Due to the quick thermalization process (discussed next), most of the electrons and holes are trapped in the lowest energy localized states and the recombination occurs between these states.
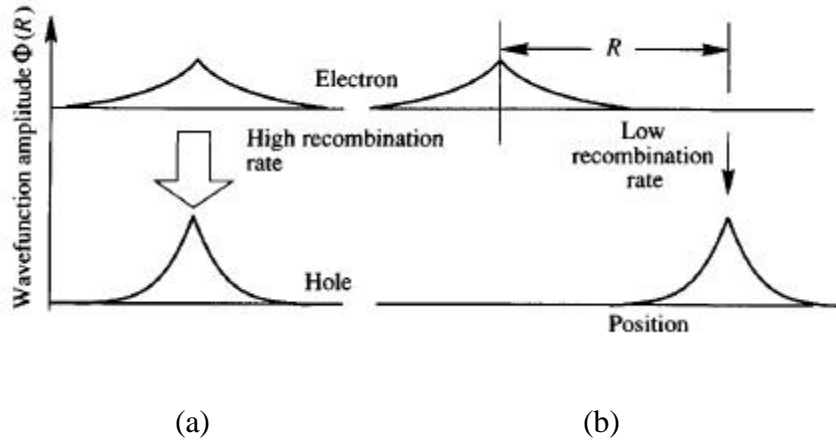
Figure 36 The dependence of recombination rate on the separation of localized waveforms (a) complete overlap (b) weak overlap [52]

As was discussed for c-Si nanoparticles, the ease of a radiative recombination process depends on the degree of overlap of the electron and hole pair. Figure 36 (a) shows an example when the wave functions overlap completely. Such a case is observed in the case of a transition between an extended and a localized state orbetween two extended states.

However, since in a-Si most of the electron and holes are trapped in localized states, the case shown in figure 36 (b) dominates. Here the trapped states are separated by a distance R which is larger than the trap localization radii (R_{0e} and R_{0h}). Assuming $R_{0e} > R_{0h}$, we can get the transition probability as :

$$P = Po \ exp(-2R/R_{Oe}) \qquad (9)$$

Where P_0 is the transition probability of completely overlapping wavefunctions. This process is called radiative tunneling and is responsible for the low temperature PL from a-Si.

Thermalization

This is a multi-step process where the energy is lost through many small but frequent inelastic transitions within the band or in the band tails. The rate of thermalization depends on the density of states, with the rate decreasing as an electron moves into localized band tail states and the density of available states decreases.

Physically, we can identify two different regimes for the process at low temperatures –

1. Thermalization in extended states is the ultrafast process which happens before the mobility edge, i.e. in the high mobility region with a lifetime of the order of 10^{-13} s. This process is governed by a large density of states, which leads to multiple, quick, small energy loss steps with the emission of single steps.

2. Tunneling between localized states becomes the dominant process below the mobility edge. Since this region is dominated by the localized band tail states and has a lower density of states compared to the extended states, thermalization rate decreases and follows an equation similar to (8). A similar process is observed in a-Si nanoparticles as discussed later.

Thermal quenching of luminescence

In this discussion, we have assumed that the a-Si is hydrogenated which lowers the defect density by saturating the dangling bonds [53]. At low temperatures, the electrons/holes remain trapped in the localize states and hence contribute to PL in spite of their rather long lifetimes.
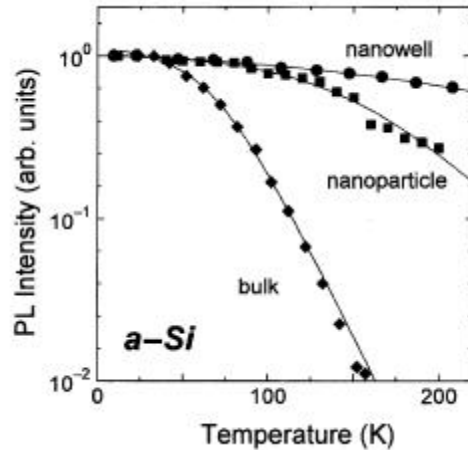
Figure 37 Temperature quenching of PL intensity with temperature for bulk, nanoparticle, nanowell a-Si [54]

However, as can be seen from the figure 37, at room temperature, the luminescence efficiency is reduced by about four orders of magnitude due to non-radiative quenching and is barely detectable. This is the major limitation of the optical response from a-Si:H.

This is because, at room temperature, the carriers have a higher mobility, since they can escape the trapped state because of their thermal energies. The defect assisted non radiative recombination has a much higher rate (almost 5 order of magnitude larger) compared to the radiative recombination. The large difference in rates means that a few non-radiative centers can completely overwhelm the radiative recombination if the carriers are sufficiently mobile to reach them. And at temperature higher than 100K the defect states are able to directly capture the electron/hole (as shown in figure 38) which due to the lower defect density were too far away to capture at low temperature. Thus, thermal quenching is observed at temperatures above which there is significant carrier transport. This is further proved by the observance of increased electrical conduction above 100K in a-Si:H which essentially correlates the increased mobility above 100K with the decreased PL.
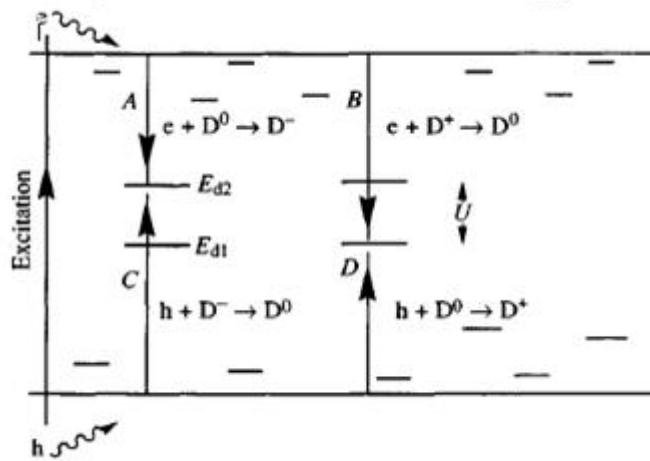
Figure 38 Electron and hole capture mechanism by the different trap states [52]

PL from a-Si:H nanoparticles

As can be seen from figure 37, the a-Si:H nanoparticles have a much improved performance at room temperature compared to bulk a-Si:H. Moreover, there have been studies which suggest a faster radiative recombination rate in a-Si nanoparticles compared to crystalline ones by comparing the corresponding recombination lifetimes [55], by using tight binding modeling [56] or experimentally in SiOx lattice (where the PL emission can be seen with a naked eye) [57].A quantum yield of close to 100% has also been shown with increasing confinement as shown in figure 39. A strong PL response from a-Si nanoparticles has also been shown in SiNx matrix by [58] or in quantum well structures. However, the studies on amorphous silicon nanoparticles are still quite less compared to crystalline silicon. Specifically, the studies of free standing a-Si nanoparticles are rather limited especially for the non-thermal plasma process. Also, not much is reported about the effect of surface passivation and the stability of hydrogen passivation to oxidation in a-Si:H nanoparticles. The possible advantages in optical output, combined with the wider

process range, lower chamber deposition and higher deposition rate for a-Si nanoparticles shown earlier, make them a very interesting material for their study.

The advances in the understanding of PL mechanisms from c-Si-Si nanoparticles have helped in the understanding of PL from a-Si nanoparticles, with surface passivation models being extended to a-Si. However, there are still some points of uncertainty regarding the mechanism of the PL from core, specifically between the quantum confinement discussed earlier and the so called spatial confinement, which are discussed in the next section.
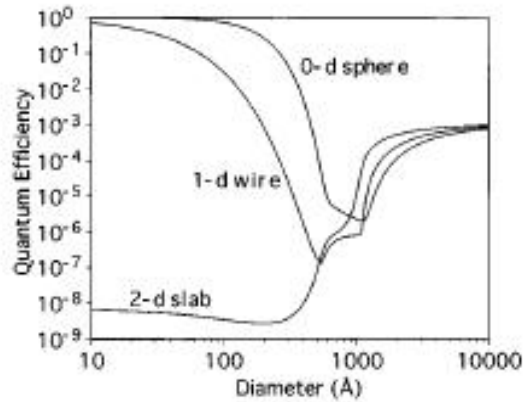
Figure 39 Theoretical calculations for improving quantum efficiencies of light emission with increased confinement in a-Si [59]

Spatial confinement

As discussed earlier, in bulk crystalline, due to the periodicity, the electron and hole wave functions are delocalized and reducing the dimensionality confines these wavefunctions fundamentally changing the band structure. However, in a-Si:H, electrons and holes are highly localized in the traps (with the localization distance of ~1 nm) and hence the reduction of dimensionality has little effect due to quantum confinement (at least for sizes larger than 2-3 nm). Thus the observed PL from a-Si:H nanoparticles at room temperatures possibly originates from a more statis2tical viewpoint called spatial

51

confinement which essentially reduces the defect mediated non radiative recombination which dominates in a-Si:H at room temperature.

In this model, the photogenerated carriers quickly thermalize to the lowest energy states within some capture radius, R_C, before recombining. Here R_C is the characteristic distance explored by an electron hole pair before its radiative recombination and is given by:

$$R_C = \frac{R_O}{2} \ln(\omega_O \tau_R) \tag{10}$$

Where R_O is the localization radius, ω_O is the escape frequency from the localization state ($\sim 10^{12}$ Hz) and τ_R is the radiative lifetime. For an R_O of 1 nm, we get an R_C of 10-12 nm in good agreement with [60]. Now, the capture volume for the electron hole pair is given by

$$V_C = \left(\frac{4}{3}\right) \pi R_c^3 \tag{11}$$

And the radiative efficiency for a single electron hole pair is given by

$$\eta i = \exp(-V_C N_D) \tag{12}$$

Where N_D is the defect density. Now, as the size of the nanoparticles is shrunk to below R_C (i.e. size <10nm), the electron hole pair get spatially confined and the V_C decreases as shown in figure 40. Quantitatively, according to equation (11) this leads to an increase in radiative efficiency. Qualitatively, as the capture volume decreases, the probability of the electron hole pair to encounter a defect state decreases due to the relatively low density of defect centers with good hydrogen passivation and confinement of electrons/holes to within a nanoparticle. This increases the radiative recombination efficiency. The equation above gives the probability of radiative recombination for only

one electron-hole pair. For a real case scenario, the net radiative efficiency is the spatial average of η_i over the volume of the nanoparticle, which on evaluation gives the curve above which predicts almost perfect quantum efficiencies (figure 39).
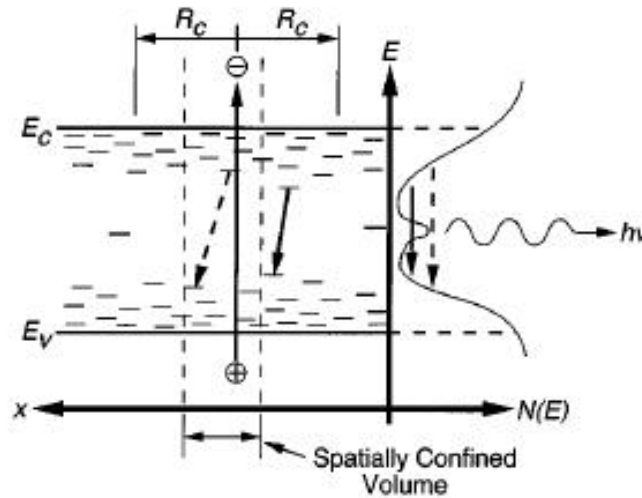
Figure 40 Energy-band diagram of confined a-Si:H photoluminescence model. Photoexcited electrons and holes recombine within a capture radius Rc [59]

Another important observation is the broad peak structure of PL in the nanoparticles compared to bulk silicon which can similarly be explained by spatial confinement. Since the distance between the deeply localized states is greater than that for the shallower localized state, as the volume of nanoparticles is spatially confined the energy of the lowest localized states available to the electron hole pair increases, increasing the bandgap. The same process will lead to a blue shift with size in spatially confined a-Si (although the blue shift is smaller compared to quantum confinement calculations), however the experiment is contradictory with some groups [61] reporting no blueshift for nanoparticles down to almost 3nm.

As was reported by [53] above the theoretical calculations for spatial confinement model predicts an excellent stability of PL against temperature, especially for particles less than 3nm.
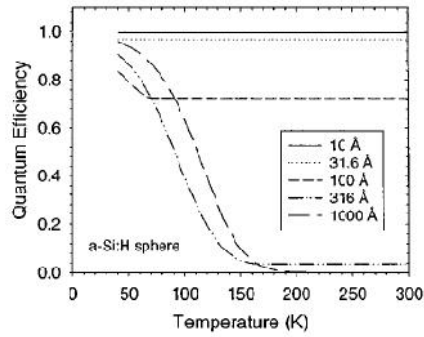
Figure 41 Theoretical calculations for temperature quenching of PL for a-Si nanoparticles of different sizes [59]

Thus, we can consider the radiative recombination from a-Si to be the overlap of two regimes

1. Spatially confined region for particles larger than 3-4nm

2. Quantum confined region (similar to crystalline nanoparticles) for smaller particles with good agreement between theory and experiment [62, 63] as shown in figure 42.
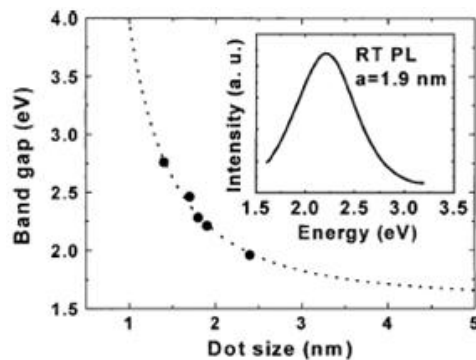
Figure 42 Theoretical model with experimental results for quantum confinement in very small a-Si nanoparticles [62]

Experimental work

As we have seen in the discussions above, the size of nanoparticle and the crystallinity are the primary factors governing the peak position of the PL; and size, crystallinity and surface passivation are the primary contributors of PL intensity. Hence in this section, we would explore the effects of these three factors on the PL response from our nanoparticles. These nanoparticles have their surface passivated by hydrogen and we would also study the stability of passivation on exposure to air and the corresponding effect on the PL response.

As discussed in [40,65] the size of the nanoparticle is governed by the residence time in the plasma: the larger the residence time, the larger the size. The residence time depends on the volume of the chamber (V), pressure (P) and the total flow rate (s) as

$$\tau \propto \frac{V.p}{s} \tag{13}$$

In our system the total flow rate and chamber pressure are dependent on each other, hence canceling out the effect of changing one of them. So, the most promising way of controlling the size is either changing the electrode position (hence changing the effective chamber length) or using multiple nozzles (a large nozzle size leads to a smaller chamber pressure for similar flow rate, leading to smaller size). The 1st option is explored in this work.

Comparison of PL from c-Si and a-Si nanoparticles

The nanoparticles were deposited on silicon wafers coated with gold, to enable the measurement of FTIR, Raman and PL spectra on the same sample. All the PL and Raman signal were collected from the same spots to eliminate variations within the samples. The PL was measured on the same Renishaw system with the 535nm laser, Si CCD camera and

300 lines/mm grating. The measured PL intensities could vary by about 10% between different days, hence they were normalized against a standard sample to be able to derive quantitative results. Experiments similar to those explained for Raman spectrum acquisition (described in chapter 3) were used to identify the optimum measurement conditions. Select samples, whose PL was measured with UV excitation on a different tool, showed similar peak positions, further confirming the measurements.

As explained above, since the residence times remain constant with changes in dilution and pressure in our chamber, the size of the nanoparticles does not change with those changes. We confirmed this using TEM images. The size distribution of the nanoparticles is shown in figure 43 for crystalline nanoparticles. The mean size of the nanoparticles is 6.47nm with a standard deviation of 0.37nm. Similar results were obtained for amorphous nanoparticles.

(a)   (b)
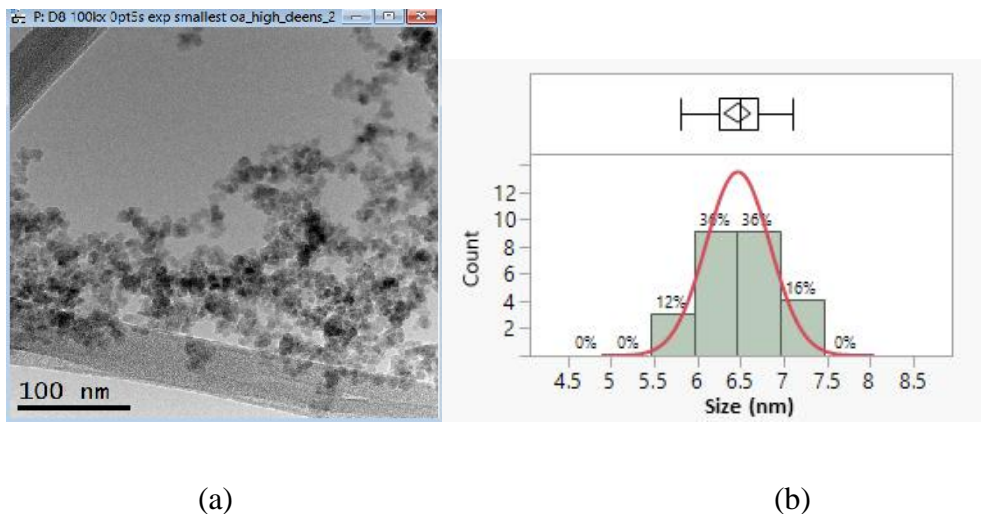
Figure 43 (a) Low magnification TEM image for crystalline nanoparticles, (b) The corresponding size distribution with mean 6.47nm and SD 0.37nm

The results in figure 44 correspond to PL from growth conditions similar to the helium dilution experiments in chapter 4. As can be seen from figure 44 (a) and (b), the PL

of the highly crystalline and completely amorphous nanoparticles were very similar among

themselves which we attribute to the similarity in their sizes and similar passivation with

H_2. This shows that the PL response does not depend directly on the flow rate and power

conditions, and these can be optimized for a high deposition rate. The PL peak position for

crystalline nanoparticles also confirms very well (correct to within 4%) for similar sized

free standing nanoparticles reported from the literature with the empirical equation [64] :

$$E \text{ (eV)} = 1.16 + \frac{11.6}{a*a} \tag{14}$$

where a is the radius of the nanoparticle in nm.

(a)

(b)

(c)
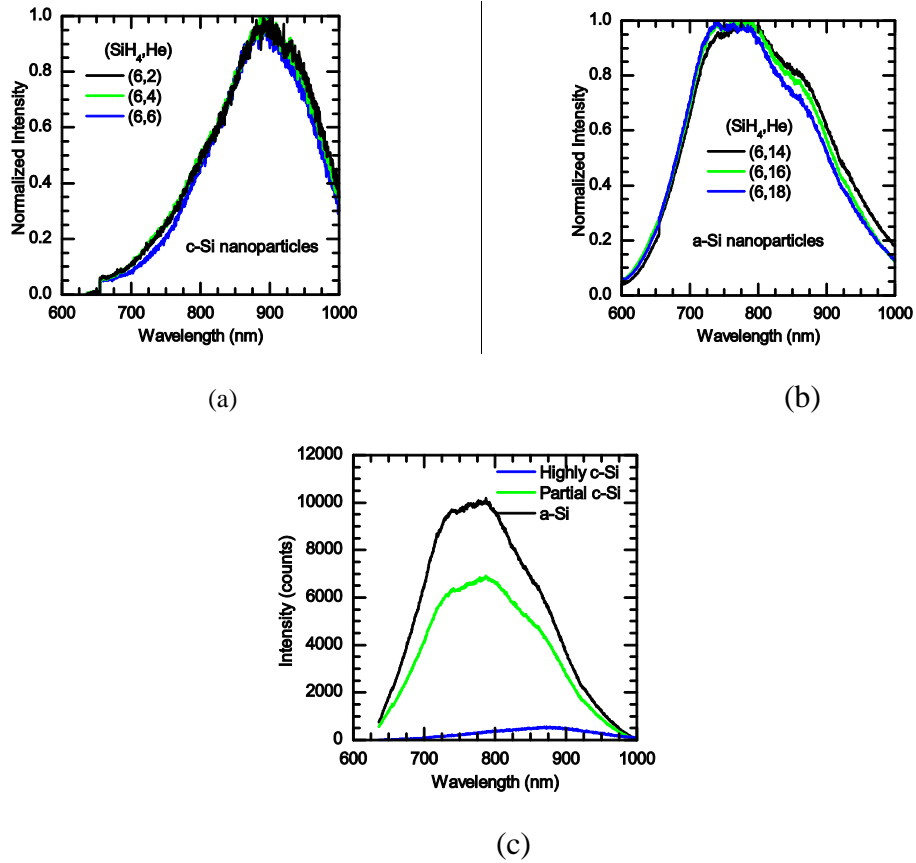
Figure 44 PL spectra for (a) high crystalline samples, (b) amorphous samples, (c) partial crystallinity

One of the few reported comparisons of free standing a-Si and c-Si nanoparticles

formed using non thermal plasma [39] reported a very weak PL from a-Si nanoparticles

which was attributed to PL from c-Si nanoparticles interspersed among a-Si nanoparticles where the amount of c-Si nanoparticles was too small to be detected by Raman spectroscopy.

However, as can be seen from figure 44 (c), the PL intensity decreases sharply with increasing crystallinity. Moreover, the peak position shifts to shorter wavelengths for amorphous silicon nanoparticles suggesting a different origin for the PL in our case, which could be due to spatial confinement discussed above.

Effect of size of nanoparticles on PL (Effect of electrode position)

<center>(1)   (2)   (3)</center>
<center>(a)</center>

<center>(b)   (c)</center>
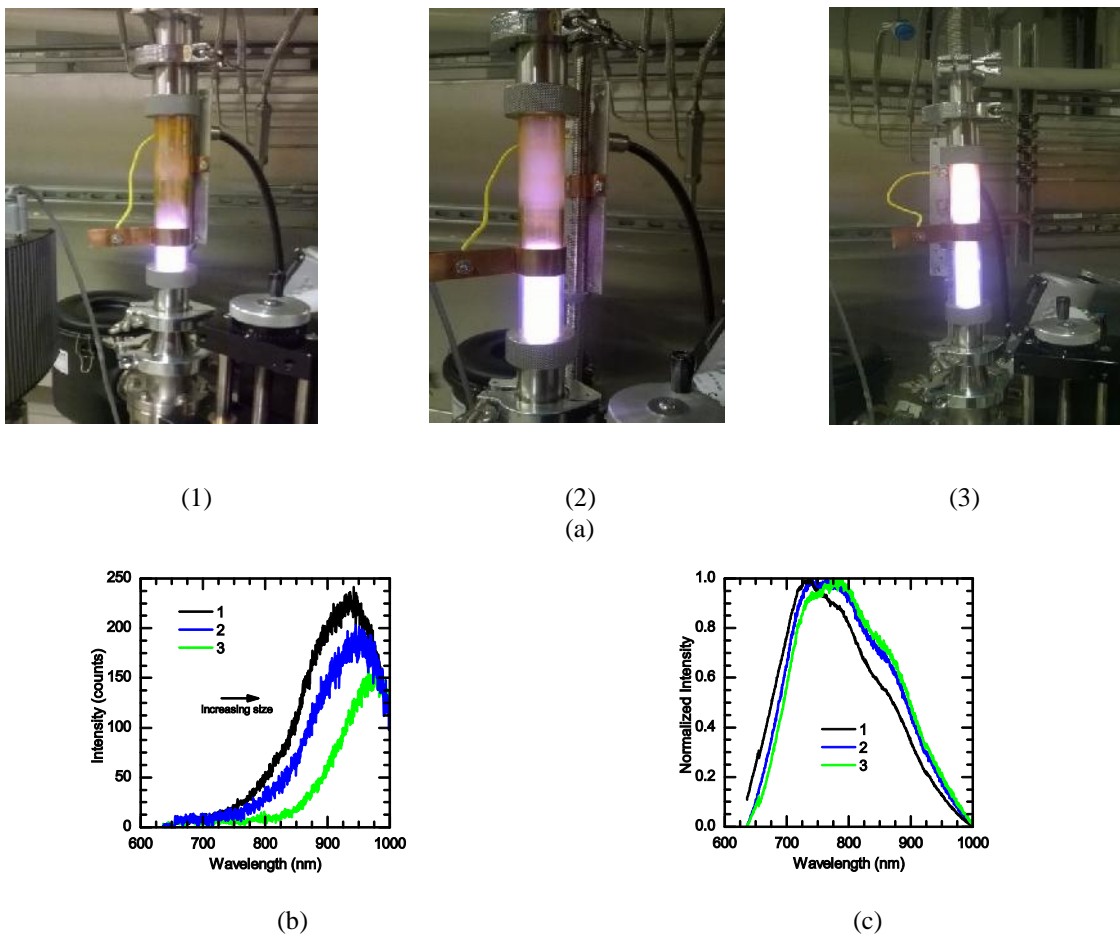
Figure 45 Experiments for control of size of nanoparticles with electrode position (a) the different electrode positions, (b) Corresponding PL curves for c-Si nanoparticles, (c) corresponding PL curves for a-Si nanoparticles.

In this set of experiments, the electrode was moved from position (1) to (3) such that plasma volume and hence, the residence time was increased. This leads to an increase in size of the nanoparticles from (1) to (3) which leads to a corresponding red shift in the peak PL wavelength along with decreasing PL intensity in accordance with the quantum confinement model (see figure 45 (b)). Hence, we can confirm the core of the nanoparticles and not the surface states as the source of PL. The Raman spectra was also measured for these 3 samples confirming them to be highly crystalline, removing differences in crystallinity as possible source of variation.

However, the nanoparticles corresponding to electrode position (1) are the smallest that can be obtained in our current setup. Hence, the use of nozzles with bigger orifices is required to obtain smaller nanoparticles and hence a higher tunability of PL wavelength to the blue region.

Extending a similar analyses to amorphous nanoparticles (figure 45(c)), we observe that no significant change in the PL structure is observed. There is a slight blue shift of peak position with decreasing size but not large enough to be explained by QC. This blue shift is attributed to the statistics of SC and suggests the SC model for our nanoparticles.

Effect of aging of nanoparticles on PL

To study the effect of aging on nanoparticles, we exposed the samples to air for over a week, and measured the changes in PL and FTIR. The measurements were done on multiple crystalline and amorphous samples and the results for 1 sample for each are shown below as representatives of amorphous and crystalline nanoparticles.

59

On studying the effect of oxidation on the PL from crystalline nanoparticles, from figure 46, we observe that the PL peak position blueshifts on oxidation. This supports the findings of some groups which suggest that the core of the nanocrystal shrinks on oxidation leading to an increased QC effect. However this is accompanied by a decreasing PL peak energy which is in contradiction with an increased QC model and contradicts the findings of some groups. The decrease in PL activity is attributed to the non-radiative states introduced at the Si-SiO$_2$ interface as the H$_2$ passivation is removed by oxidation. This is also confirmed by the decreasing SiH$_x$ peak shown in the FTIR spectrum in (c).

(a)

(b)

(c)

Figure 46 Effect of exposure to air on c-Si nanoparticles (a) absolute intensity of on different days, (b) normalized intensity, (c) Corresponding FTIR spectrum

From figure 47, a-Si nanoparticles do not experience any change in their PL profile and only the intensity is reduced. The lack of shift in PL peak position is considered as a further proof of the absence of QC in a-Si nanoparticles in the size regime of our nanoparticles.We attribute the decrease in internsity to the creation of non-radiative recombination surface states upon oxidation. However it should be noted that the although the PL intensity dropped to less than half in the case of c-Si nanoparticles, the decrease is much less drastic in the case of a-Si nanopaarticles pointing to a better passivation.
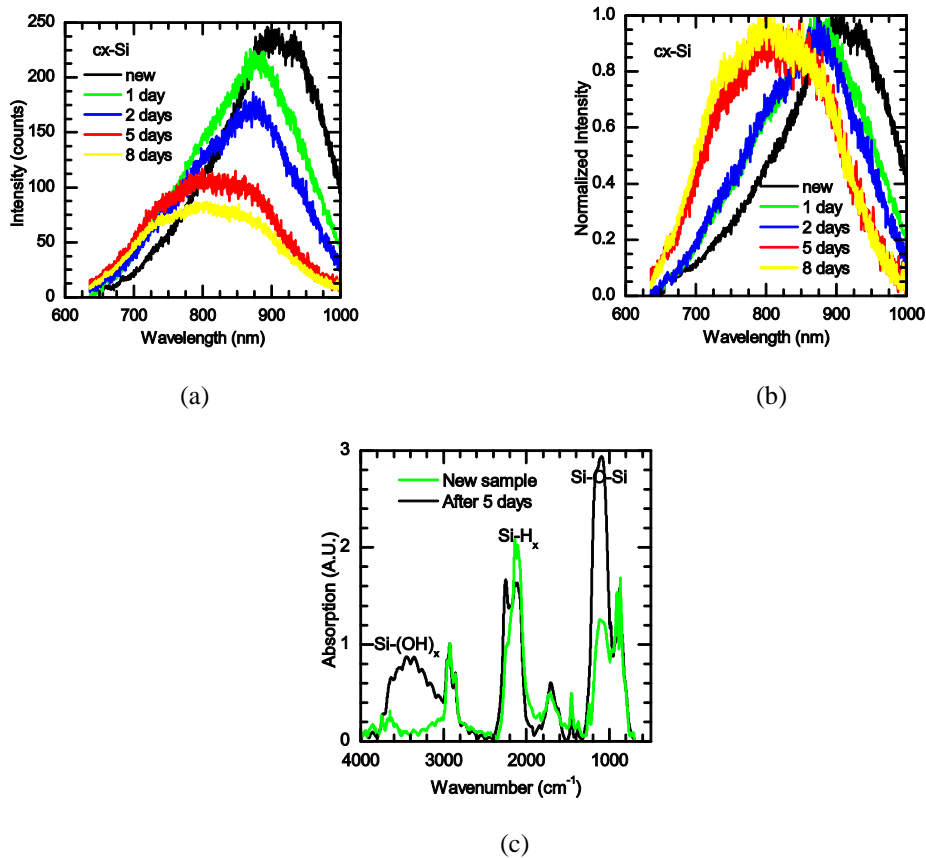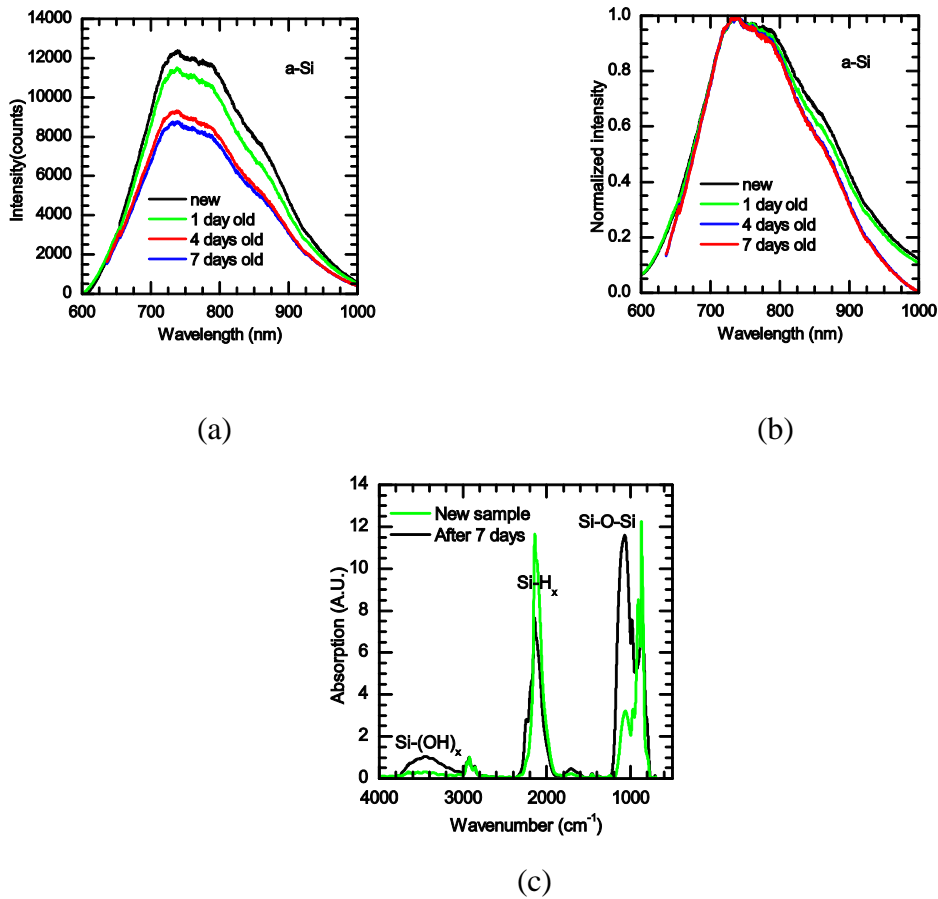

(a)

(b)

(c)

Figure 47 Effect of exposure to air on a-Si nanoparticles (a) absolute intensity of on different days, (b) normalized intensity, (c) Corresponding FTIR spectrum

The PL curves suggest that the oxidation process is self limiting with further decay in PL stopping after a few days. The self limiting is also confirmed by experiments where several week old samples were annealed at 100^OC for 30 minutes. There was no observable changes in PL, although anneal experiments at higher temperatures need to be done in the future to evaluate the stability of H_2 passivation to temperature.

This is further proved by the measurement of evolution of the Si-O-Si FTIR peak with respect to the initial Si-H_x peak. As we see in figure 48, the passivation is poorer in the case of crystalline silicon with the number of Si-H passivating bonds lost to oxidation being almost twice the case of a-Si. This also explains the the almost 60% decay in PL of the crystalline nanoparticles. However, bulk a-Si has hydrogen atoms incorporated within the silicon network and not only on the surface. A similar structure in a-Si nanoparticles might lead to errors to quantitative estimation of H-passivation stability.

Hence the higher PL intensity (almost 50 times higher), better passivation and larger growth window of a-Si silicon nanoparticles make it a promising competitor to crystalline silicon nanoparticles. However, the lack of tunability of the PL from a-Si nanoparticles remains an issue to be addressed by using larger nozzles to grow nanoparticles which are less than 3nm in size.
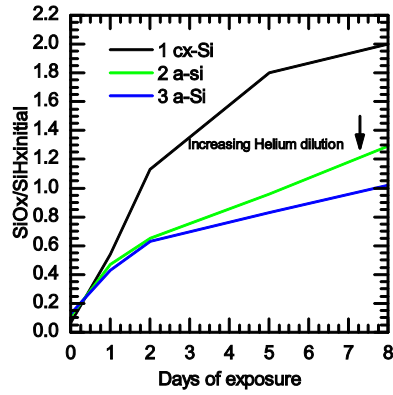
Figure 48 Comparison of passivation of c-Si-Si and a-Si nanoparticles by comparing the ratio of peak intensities of Si-O-Si peak and the intitial SiH_x peaks on each sample. The He flow rate is increasing on going from 1 to 3

Chapter 6

FUTURE WORK

In this work, a tool for plasma deposition of silicon nanoparticles was developed. A high PL response from amorphous silicon nanoparticles and the stability of surface passivation with hydrogen was explored and quantified. Quantum confinement and spatial confinement in crystalline and amorphous nanoparticles respectively was demonstrated.

The future work would be divided into the following sections:

1. TOOL IMPROVEMENT

   (A) Currently the motion control, the process valve, power source and atmospheric vent are all manually controlled. In the near future these would be automated with development of appropriate hardware and software.

   (B) Anny and Deppy share the same computer for control right now due to shared components for MFC and pneumatic valve control. These would be decoupled for a truly parallel operation of the two tools.

   (C) The control over size of nanoparticles is rather limited due to the lack of a tunable nozzle. A set of nozzles with varying orifices would be integrated into the tool, improving its tunability.

   (D) Chamber heating prevents the use of high power deposition conditions. Active chamber cooling would be explored.

   (E) In-Situ Raman/PL in Deppy

   Deppy has an optical fiber extension from the Renishaw tool which can be used for in-situ Raman and PL measurements of samples from Anny and Deppy to study the effect of high temperature processes on PL quantum yield and

correlate the loss in H_2 during annealing (measured through in-situ FTIR) on the PL.

The LabVIEW code (figure 49) for the focusing of the sample using incremental z-stage movement of Deppy, fine up to 0.1 mm incremental steps has been developed and confirmed to work for Raman measurements. This code also has checks to stop further movement when the chuck is at the highest/lowest points and resets the value to deposition defaults after the measurements are completed. The development of a permanent fixture for the probe would enable quick measurements.
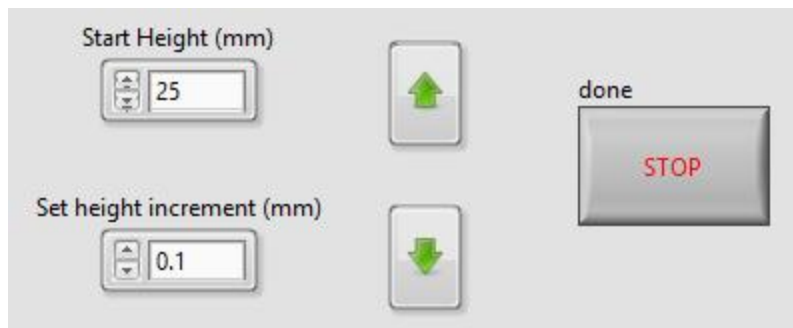
Figure 49 LabVIEW code for in-situ Raman measurements

(F) Exploration of electrode design for inductively coupled plasma

2. PLASMA CHARACTERIZATION

Currently, we cannot probe the plasma to identify the active species and electric fields inside the chamber. Utilization of RGA and redesign of chamber compatible with a Langmuir probe would be explored.

3. APPLICATIONS OF a-Si NANOPARTICLES

a-Si nanoparticles have been demonstrated to possess favorable absorption and emission characteristics. Demonstration of the applications using electroluminescence for LEDs and as redshifter in solar cells would be explored.

REFERENCES

[1] http://semimd.com/petes-posts/2014/07/14/can-we-take-cost-out-of-technology-scaling/

[2] Francesco Priolo, Tom Gregorkiewicz, Matteo Galli and Thomas F. Krauss; Silicon nanostructures for photonics and photovoltaics; *Nature Nanotechnology* 9,19–32 (2014)

[3] L. Mangolini; Synthesis, properties, and applications of silicon nanocrystals; J. Vac. Sci. Technol. B 31, 020801 (2013); doi: 10.1116/1.479478

[4] W. Arden, M. Brillouët, P. Cogez, M. Graef, B. Huizing and R. Mahnkopf; More-than-Moore White Paper; International Technology Roadmap for Semiconductors (2013)

[5] L. T. Canham; Silicon quantum wire array fabrication by electrochemical and chemical dissolution of wafers; Appl. Phys. Lett. 57, 1046 (1990)

[6] S. Prezioso, A. Anopchenko, Z. Gaburro, L. Pavesi, G. Pucker, L. Vanzetti and P. Bellutti; Electrical conduction and electroluminescence in nanocrystalline silicon-based light emitting devices; J. Appl. Phys. 104, 063103 (2008)

[7] R. J. Waters, G. I. Bourianoff and H. A. Atwater; Field-effect electroluminescence in silicon nanocrystals; Nature Materials 4, 143 - 146 (2005)C. B. Murray, D. J. Norris and M. G. Bawendi; Synthesis and characterization of nearly monodisperse CdE (E = sulfur, selenium, tellurium) semiconductor nanocrystallites; *J. Am. Chem. Soc.*, 115 (19), pp 8706–8715 (1993)

[8] M. Hirasawa, T. Orii and T. Seto; Size-dependent crystallization of Si nanoparticles; *Appl. Phys. Lett.*88 093119 (2006)

[9] K. A. Littau, P. J. Szajowski, A. J. Muller, A. R. Kortan and L. E. Brus; A luminescent silicon nanocrystal colloid via a high-temperature aerosol reaction; *J. Phys. Chem.* 97 1224–30 *(1993)*

[10] P. E. Batson and J. R. Heath; Electron energy loss spectroscopy of single silicon nanocrystals: the conduction band *Phys. Rev. Lett.* 71 911–14 (1993)

[11] G. Ledoux, J. Gong, F. Huisken, O. Guillois and C. Reynaud; Photoluminescence of size-separated silicon nanocrystals: Confirmation of quantum confinement; Appl. Phys. Lett. 80, 4834 (2002)

[12] L Boufendi and A Bouchoule; Particulate formation and dusty plasma behaviour in argon–silane RF discharge; *Plasma Sources Sci. Technol.* 2 204 (1993)

[13] L Boufendi and A Bouchoule; Particle nucleation and growth in a low-pressure argon-silane discharge; Plasma Sources Sci. Technol. 3 *262-267 (1994)*

[14] A. A. Fridman, L. Boufendi, T. Hbid, B. V. Potapkin, and A. Bouchoule; Dusty plasma formation: Physics and critical phenomena. Theoretical approach; Journal of Applied Physics 79, 1303 (1996)

[15] U. Kortshagen; Nonthermal plasma synthesis of semiconductor nanocrystals; J. Phys. D: Appl. Phys. 42 113001 (22pp) (2009)

[16] Y. Watanabe; Formation and behaviour of nano/micro-particles in low pressure plasmas *J. Phys. D: Appl. Phys.* 39 R329 (2006)

[17] J. Perrin, C. Bohm, R. Etemadi and A. Lloret; Possible routes for cluster growth and particle formation in RF silane discharges *Plasma Sources Sci. Technol.* 3 252 (1994)

[18] L.Mangolini and U. Kortshagen; Selective nanoparticle heating: another form of nonequilibirium in dusty plasmas *Phys. Rev.* E 79 026405 (2009)

[19] Application Note – Working with Thermal-based Mass Flow Controller Gas Correction Factors c/o Scribner Associate Incorporated

[20] http://www.mksinst.com/docs/ur/MFCGasCorrection.aspx (online)

[21] B. Schrader; Infrared and Raman Spectroscopy, Methods and Applications; (1995)

[22] P. Larkin; Infrared and Raman Spectroscopy Principles and Spectral Interpretation; (2011)

[23] https://en.wikipedia.org/wiki/Raman_scattering

[24] G. Viera, S. Huet, and L. Boufendi; Crystal size and temperature measurements in nanostructured silicon using Raman spectroscopy; Journal of Applied Physics 90, 4175 (2001)

[25] http://chemwiki.ucdavis.edu/Physical_Chemistry/Spectroscopy/Vibrational_Spect roscopy/Infrared_Spectroscopy/How_an_FTIR_Spectrometer_Operates (online)

[26] Introduction to Fourier Transform Infrared Spectrometry; c/o Thermo Nicolet Corporation

[27] R. Spragg; Reflection measurements in IR spectroscopy; c/o PerkinElmer, Inc.

[28] A. P. Alivisatos; Semiconductor Clusters, Nanocrystals, and Quantum Dots; Science, New Series, Vol. 271, No. 5251, 933-937 (1996)

[29] L. Brus; Electronic wave functions in semiconductor clusters: experiment and theory; *J. Phys. Chem.*, *90* (12), pp 2555–2560 (1986)

[30] D. Vanmaekelbergh and P. Liljeroth; Electron-conducting quantum dot solids: novel materials based on colloidal semiconductor nanocrystals; *Chem. Soc. Rev.*, 2005,34, 299-312

[31] G. D. Sanders and Y. C. Chang; Theory of optical properties of quantum wires in porous silicon; Phys. Rev. B 45, 9202 – Published 15 April 1992

[32] Y. M. Niquet, C. Delerue, G. Allan, and M. Lannoo; Method for tight-binding parametrization: Application to silicon nanostructures; Phys. Rev. B 62, 5109 (2000)

[33] A. Zunger; Pseudopotential Theory of Semiconductor Quantum Dots; physica status solidi (b) Volume 224, Issue 3, pages 727–734; 2001

[34] G. Bester; Electronic excitations in nanostructures: an empirical pseudopotential based approach; *J. Phys.: Condens. Matter* 21 023202 (2009)

[35] E. G. Barbagiovanni, D. J. Lockwood, P. J. Simpson and L. V. Goncharova; Quantum confinement in Si and Ge nanostructures: Theory and experiment; Appl. Phys. Rev. 1, 011302 (2014)

[36] G. Ledoux, J. Gong, F. Huisken, O. Guillois and C. Reynaud; Photoluminescence of size-separated silicon nanocrystals: Confirmation of quantum confinement; Appl. Phys. Lett. 80, 4834 (2002)

[37] C. Meier, A. Gondorf, S. Lüttjohann, and A. Lorke; Silicon nanoparticles: Absorption, emission, and the nature of the electronic bandgap; JOURNAL OF APPLIED PHYSICS 101, 103112 (2007)

[38] T. Makimura, Y. Kunii, N. Ono, K. Murakami; Silicon nanoparticles embedded in SiO films with visible 2Photoluminescence; Applied Surface Science 127–129 . 388–392 (1998)

[39] Y. H. Xie, W. L. Wilson, F. M. Ross, J. A. Mucha, E. A. Fitzgerald, J. M. Macaulay and T. D. Harris; Luminescence and structural study of porous silicon films; J. Appl. Phys. 71, 2403 (1992)

[40] R. Anthony and U. Kortshagen; Photoluminescence quantum yields of amorphous and crystalline silicon nanoparticles; Phys. Rev. B 80, 115407 (2009)

[41] X. Li , Y. He , S. S. Talukdar , and M. T. Swihart; Process for Preparing Macroscopic Quantities of Brightly Photoluminescent Silicon Nanoparticles with Emission Spanning the Visible Spectrum; *Langmuir*, *19* (20), pp 8490–8496 (2003)

[42] X. Li , Y. He ,and M. T. Swihart; Surface Functionalization of Silicon Nanoparticles Produced by Laser-Driven Pyrolysis of Silane followed by HF–HNO$_3$ Etching; *Langmuir*, 20 (11), pp 4720–4727 (2004)

[43] A. Gupta, H. Wiggers; Surface chemistry and photoluminescence property of functionalized silicon nanoparticles; hysica E 41 1010–1014 (2009)

[44] D. Comedi, O. H. Y. Zalloum, E. A. Irwing, J. Wojcik, P. Mascher; H-induced effects in luminescent silicon nanostructures obtained from plasma enhanced chemical vapor deposition grown Si$yO1-y$:$H(y>1⁄3)$ thin films annealed in (Ar+5%$H2$); J. Vac. Sci. Technol. A 24, 817 (2006)

[45] M. B. Robinson, A. C. Dillon, D. R. Haynes and S. M. George; Effect of thermal annealing and surface coverage on porous silicon photoluminescence; Appl. Phys. Lett. 61, 1414 (1992)

[46] R. T. Collins, M. A. Tischler and J. H. Stathis; Photoinduced hydrogen loss from porous silicon ; Appl. Phys. Lett. 61, 1649 (1992)

[47] B. G. Fernandez, M. López, C. Garcıa, A. P. Rodrıguez, J. R. Morante, C. Bonafos, M. Carrada and A. Claverie; Influence of average size and interface passivation on the spectral emission of Si nanocrystals embedded in SiO2; J. Appl. Phys. 91, 798 (2002)

[48] S. M. Prokes, W. E. Carlos and V. M. Bermudez; Luminescence cycling and defect density measurements in porous silicon: Evidence for hydride based model; Appl. Phys. Lett. 61, 1447 (1992)

[49] M. V. Wolkin, J. Jorne, P. M. Fauchet, G. Allan, and C. Delerue; Electronic States and Luminescence in Porous Silicon Quantum Dots: The Role of Oxygen; Phys. Rev. Lett. 82, 197 (1999)

[50] A. Puzder, A. J. Williamson, J. C. Grossman, and G. Galli; Surface Chemistry of Silicon Nanoclusters; Phys. Rev. Lett. 88, 097401 (2002)

[51] D. Weaire and M. F. Thorpe; Electronic Properties of an Amorphous Solid. I. A Simple Tight-Binding Theory; Phys. Rev. B 4, 2508 (1971)

[52] R. A. Street; Hydrogenated amorphous silicon; (1991)

[53] W. Paul, D.A. Anderson; Properties of amorphous hydrogenated silicon, with special emphasis on preparation by sputtering; Solar Energy Materials 5, 229-316 (1981)

[54] Y. Kanemitsu; Efficient light emission from crystalline and amorphous silicon nanostructures; Journal of Luminescence 100 209–217 (2002)

[55] M. Stutzmann; The defect density in amorphous silicon; Philos. Mag. B, Vol. 60, No. 4, 531-546 (1989)

[56] K. Nishio, J. K ga, T. Yamaguchi, and F. Yonezawa; Theoretical study of light-emission properties of amorphous silicon quantum dots; Phys. Rev. B 67, 195304 (2003)

[57] D. Nesheva, C. Raptis, A. Perakis, I. Bineva, Z. Aneva, Z. Levi, S. Alexandrova and H. Hofmeister; Raman scattering and photoluminescence from Si nanoparticles in annealed SiOx thin films; J. Appl. Phys. 92, 4678 (2002)

[58] Y. Q. Wang, Y. G. Wang, L. Cao and Z. X. Cao; High-efficiency visible photoluminescence from amorphous silicon nanoparticles embedded in silicon nitride; Appl. Phys. Lett. 83, 3474 (2003)

[59] M. J. Estes and G. Moddel; Luminescence from amorphous silicon nanostructures; Phys. Rev. B, Vol. 54, No. 20 (1996)

[60] The random-phase model in non-crystalline systems; N.F. Mott; Philos. Mag. B 43, 941 (1981)

[61] R.B. Wehrspohn, J.-N. Chazalviel, F. Ozanam, I. Solomon; Spatial versus quantum confinement in porous amorphous silicon nanostructures; Eur. Phys. J. B8, 179-193 (1999)

[62] N. M Park, C. J. Choi, T. Y. Seong and S. J. Park; Quantum Confinement in Amorphous Silicon Quantum Dots Embedded in Silicon Nitride; Phys. Rev. Lett. 86, 1355 (2001)

[63] K. Nishio, J. Koga, T. Yamaguchi and F. Yonezawa; Light emission properties of amorphous silicon quantum dots; Journal of Non-Crystalline Solids, Vol 312–314, 323–326 (2002)

[64] T. Y. Kim, N. M. Park, K. H, Kim, G. Y. Sung, Y. W. Ok, T. Y. Seong and C. J. Choi; Quantum confinement effect of silicon nanocrystals *in situ* grown in silicon nitride films; Appl. Phys. Lett. 85, 5355 (2004)

[65] L. Mangolini, E. Thimsen, and U. Kortshagen; High-Yield Plasma Synthesis of Luminescent Silicon Nanocrystals; Nano Letters Vol. 5, No. 4 655-659 (2005)